

Defects induce phase transition from dynamic to static rippling in graphene

Fabian L. Thiemann,^{1,2, a)} Camille Scalliet,³ Erich A. Müller,⁴ and Angelos Michaelides^{2, b)}

¹⁾ IBM Research Europe, Keckwick Lane, Daresbury, WA4 4AD, United Kingdom

²⁾ Yusuf Hamied Department of Chemistry, University of Cambridge, Lensfield Road, Cambridge, CB2 1EW, United Kingdom

³⁾ Laboratoire de Physique de l'Ecole Normale Supérieure, ENS, Université PSL, CNRS, Sorbonne Université, Université de Paris, F-75005 Paris, France

⁴⁾ Department of Chemical Engineering, Sargent Centre for Process Systems Engineering, Imperial College London, South Kensington Campus, London SW7 2AZ, United Kingdom

(Dated: June 10, 2024)

Many of graphene's remarkable properties are intrinsically linked to its inherent ripples. Defects, whether naturally present or artificially introduced, are known to have a strong impact on the rippling of graphene. However, how defects alter ripple dynamics in two-dimensional (2D) materials in general, and graphene in particular, remains largely unexplored. Here, using machine learning-driven molecular dynamics simulations, we reveal a fundamental connection between defect concentration and ripple dynamics in freestanding graphene sheets. Specifically, we find that at a critical concentration of approximately 0.1%, dynamic rippling undergoes a transition from freely propagating to static ripples. This is in quantitative alignment with the experimentally observed turning point in the non-monotonic scaling of the Young's modulus and emphasises the critical interplay between defects and material dynamics. Our work not only unveils the significant impact of defects on rippling dynamics in graphene but also paves the way to design two-dimensional devices with tailored properties.

I. INTRODUCTION

Although commonly described as flat, two-dimensional (2D) graphene owes its existence,¹ as well as many of its unique properties,²⁻⁵ to the presence of intrinsic ripples at the nanoscale.^{6,7} Like crumpling a piece of paper affects its stiffness,⁸ ripples shape the mechanical and electronic behaviour of graphene. For instance, these atomic height undulations are critical to phenomena such as electron-hole puddle formation,^{9,10} suppression of weak localisation,¹¹ enhanced chemical reactivity,¹²⁻¹⁴ and motion of adsorbates^{15,16} across the surface.

Owing to this broad importance, and the central role of graphene as the first and the prototype 2D material, extensive research has been conducted on both the structural characteristics, such as amplitude or overall corrugation,^{6,17-22} and the dynamic behaviour of these fluctuations in pristine free-standing graphene.²³⁻²⁹ Much of this work has been done out of sheer scientific curiosity but also with the goal of modifying the out-of-plane deviations to invoke desired material properties. Notably, a series of scanning tunneling microscopy (STM) experiments^{24,25} revealed a diverse spectrum of dynamic patterns spanning from random fluctuations to periodic oscillations and large jumps known as 'mirror-buckling' which correspond to rapid curvature inversions in membranes subject to compressive strains. Remarkably, these rippling modes can be induced and modified using external stimuli such as electric currents,²⁴ temper-

ature gradients,³⁰ or laser pulses^{26,27} opening up exciting possibilities for advanced material design.

Despite the significance of these findings, the dynamic behaviour of ripples in the presence of defects, either introduced during manufacturing or intentionally added, remains unexplored. Atomic defects offer a unique opportunity to generate strains at the local scale and induce tailored dynamic patterns, possibly richer than those caused by global strains. Previous work has primarily focused on the structural impact of defects, revealing an out-of-plane buckling of the surface and a consistent increase in the corrugation of graphene.³¹⁻³⁴ Understanding how defects influence rippling dynamics, however, could provide explanations for puzzling experimental observations, such as the vanishing thermal expansion coefficient,³⁵ and could help reconcile conflicting findings regarding the mechanical stiffness of defective graphene. While several experiments^{36,37} find a reduction in the Young's modulus with increasing defect concentration, López-Polín et al.^{38,39} reported a non-monotonic relationship, suggesting that a specific defect density can lead to mechanical stiffening. Beyond unraveling these scientific mysteries, controlling the rippling dynamics could open new avenues to develop innovative nanotechnologies through defect engineering. With recent reports on *trampoline* dynamics preventing proteins from unfolding,⁴⁰ predictions of rippling-accelerated molecular transport,^{15,16} and findings that ripples enable graphene to split molecular hydrogen orders of magnitude faster than the best catalysts,¹⁴ this knowledge could lay the foundations for the design of 2D nano-devices where both the catalytic and adsorbate behaviour is controlled by the introduction of defects.

Here, we employ large scale machine learning-driven

^{a)} Electronic mail: fabian.thiemann@ibm.com

^{b)} Electronic mail: am452@cam.ac.uk

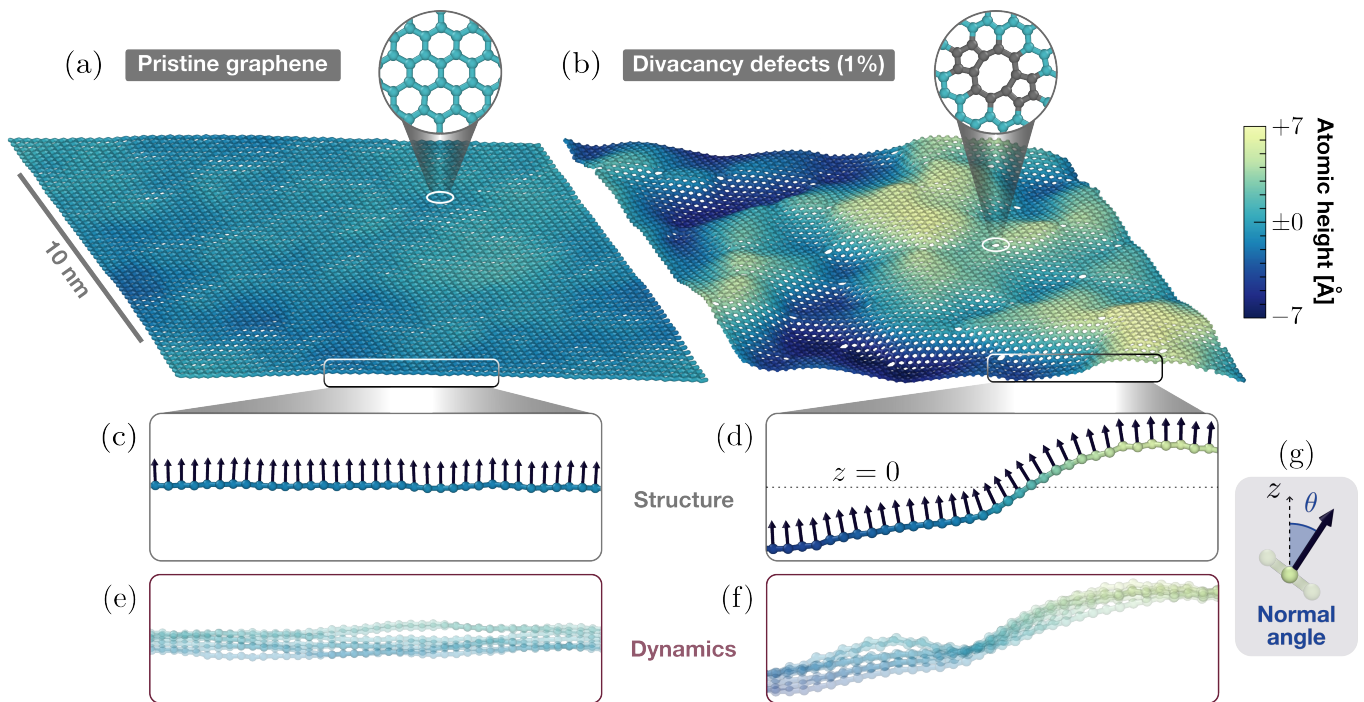


Figure 1. **Impact of atomic defects on the structure and dynamics of free-standing graphene.** The atoms in (a) pristine and (b) defective free-standing graphene are coloured according to their out-of-plane position relative to the center of mass of the respective system. The latter contains 1% divacancy defects (inset). We characterize the structure (c, d) and dynamics (e, f) of graphene via the local inclination θ , defined in panel (g) as the angle between the normal vector (arrows) and the z direction. The side-view cuts of (c, e) pristine and (d, f) defective samples are shown with the same field of view. Defects have a profound influence not only on the static corrugation of graphene, but also on its dynamic fluctuations. This is illustrated in panels (e, f) where snapshots captured at consecutive times, separated by 1 ps, are superimposed. While the pristine sheet evolves freely in (e), dynamic fluctuations are highly constrained by the presence of defects (f).

molecular dynamics (MD) simulations to explore the impact of atomic defects on the rippling dynamics of free-standing graphene sheets across defect concentrations, up to 1%. Among the various atomic defects identified in graphene,⁴¹ our focus lies on 5-8-5 divacancies. They result from the loss of two adjacent carbon atoms, induced for example via electron or ion beam irradiation.^{42–45} The reconstruction of the carbon sp^2 network creates an atomic defect comprising an eight-membered ring surrounded by two five-membered rings, as depicted in the inset of Fig. 1(b). These atomic defects are particularly well-suited for our investigation because they do not migrate,⁴⁶ and their effect on corrugation is much stronger³⁴ than other types of divacancies⁴⁷ or the topological Stone-Wales defect.⁴⁸

While our main focus is on the dynamics, understanding the impact of defects on ripples necessitates an initial examination of graphene’s corrugation as a function of defect concentration. For this purpose, we propose an approach based on assessing the average deviation of the surface normal from its mean direction, referred to as root mean square (rms) normal angle or inclination, enabling a comparison to transmission electron microscopy (TEM) diffraction patterns^{6,20,22} of pristine

graphene. While we confirm the previously observed trend of an enhanced corrugation with increasing defect concentration,^{34,49} our data based on the rms inclination reveals a discontinuity at low defect concentrations of $\approx 0.1\%$. By analysing the fluctuations of the rms inclination over time, we find this discontinuity is of dynamic nature, suggesting a disorder-induced dynamic transition from freely propagating ripples to frozen and static buckling. The critical defect concentration coincides quantitatively with the experimentally observed turning point of the non-monotonic scaling of the Young’s modulus with the density of defects.³⁸ Going beyond this fundamental insight, our local analysis of surface normal fluctuations provides valuable insights into how to tune ripple dynamics, offering prospects for designing tailor-made nanodevices.

II. RESULTS AND DISCUSSION

Starting with general observations, in Fig. 1 we present snapshots of pristine (a,c,e) and defective graphene containing 1% divacancies (b,d,f). In the Supplementary Information (SI), we also provide movies of pristine graphene and selected defective systems. Freely

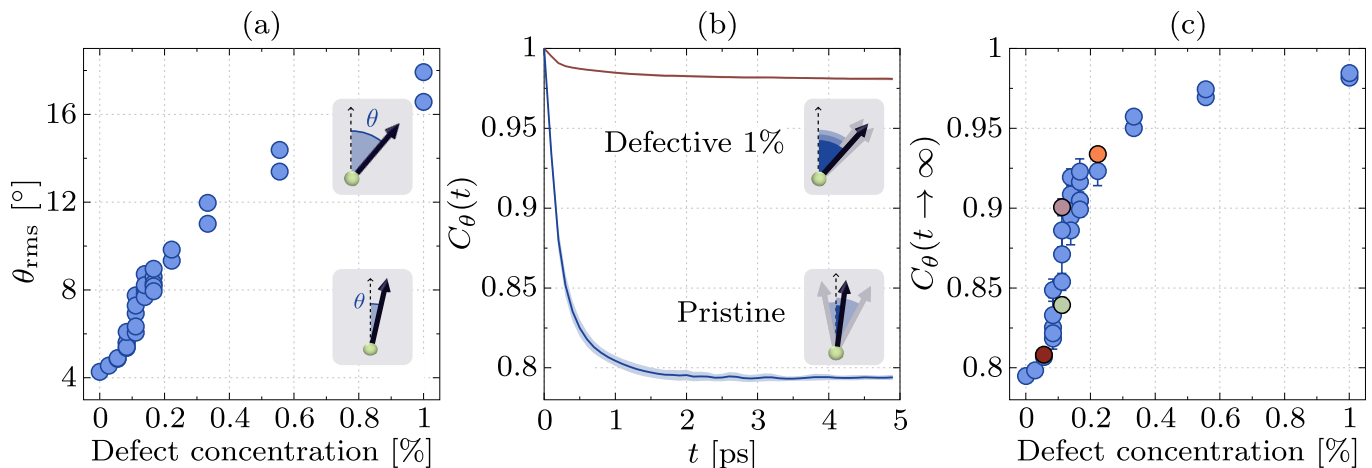


Figure 2. **Static and dynamic transition in graphene rippling with increasing defect concentration.** (a) Evolution of the root-mean-square inclination θ_{rms} with defect concentration. (b) Normalised inclination time-correlation function $C_\theta(t)$ in pristine and highly defective graphene. (c) Long-time inclination correlation as a function of defect concentration. At any concentration, the various data points correspond to different defect arrangements (positions, orientations). We observe a transition from dynamic to static rippling around a defect concentration of 0.1%. Fig. 3 depicts snapshots of the local $C_\theta(t)$ in the systems highlighted by colored data points reported in panel (c).

suspended graphene⁶ at room temperature is naturally corrugated, with atomic out-of-plane positions deviating from the centre of mass position $z = 0$, where z is the direction perpendicular to the sheet. In the presence of defects, however, the corrugation is significantly greater compared to that induced by thermal fluctuations, as shown in Fig. 1(a-d), which uses the same color scale for both pristine and defective graphene. Beyond the deviations in the static structure, we observe a critical influence of defects on the dynamics of graphene as evident from Fig. 1(e, f) where we show a superposition of side-views of snapshots at successive times. Individual snapshots are slightly transparent, such that dynamic regions of the samples appear blurred, while static regions are brighter. Pristine graphene displays high flexibility allowing each atom to explore the full range of accessible out-of-plane (z) positions, indicating random and short-lived height fluctuations. In stark contrast, the highly defective system (right) exhibits fluctuations around the induced corrugation pattern, suggesting confinement in a local free energy minimum and static buckling.

To comprehend these differences in the rippling behaviour, we now quantitatively explore corrugation and dynamics; with the key results summarised in Fig. 2. We first discuss the impact of defects on the static corrugation based on the root mean square (rms) inclination θ_{rms} . We present its dependence with defect concentration in Fig. 2(a). This observable directly informs on the range of local inclinations accessible to the sheet, see the Methods section for details. The pristine sheet serves as baseline for which we find $\theta_{\text{rms}} \approx 4.2^\circ$ agreeing well with the experimental value, $\theta_{\text{rms}}^{\text{exp}} \approx 5.0^\circ$, derived from electron diffraction patterns.^{6,20,22} Notably,

recent measurements²² indicate variations in corrugation based on manufacturing, with CVD-grown graphene showing double the corrugation of mechanically exfoliated graphene, possibly due to static wrinkles. While experimental reports of the rms inclination are limited to pristine graphene, here we report how this measure depends on defect concentration. We observe a substantial increase in θ_{rms} as the number of defects rises, reaching an inclination of $\approx 17^\circ$, i.e. roughly four times larger than the pristine case, for the largest defect concentration studied of 1%. These observations align with our prior computational study.³⁴ However, in contrast with the previously reported steady increase in corrugation with defect concentration, our choice of observable enables us to identify a sharp increase in the rms inclination at low defect concentration. We reveal in Fig. S12 of the SI that the jump gets sharper with increasing system size. Specifically, the largest variance across different spatial arrangements is observed at a defect concentration of $\approx 0.1\%$.

Motivated by these findings, we investigate whether the observed static discontinuity influences the dynamical behavior. In Fig. 2(b) we show the normalised autocorrelation functions of the normal angle, $C_\theta(\tau)$, for a pristine sample and graphene with a defect concentration of 1%. A comprehensive overview of all systems studied can be found in section S2.A of the SI. For both systems, $C_\theta(\tau)$ decays exponentially to distinct plateau values within a few picoseconds. The plateau value, or long-time inclination correlation, denoted $C_\theta(\tau \rightarrow \infty)$, quantifies how much atomic inclinations are correlated over time. Higher values suggest a more constrained local inclination and static rippling, while lower values indicate greater flexibility and dynamic rippling (see

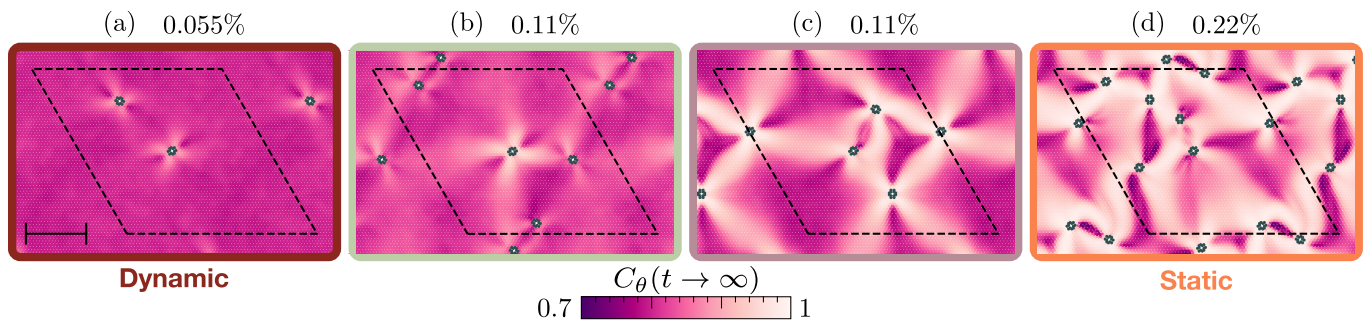


Figure 3. **Spatially heterogeneous dynamics in defective graphene.** Atomically resolved long-time inclination correlation $C_\theta(\tau \rightarrow \infty)$ for selected samples whose mean correlation is reported with colored points in Fig. 2(c) (referred to by frame color). The correlation increases from (a) to (d). The defect concentration corresponding to each snapshot is reported next to the labels. Defects are highlighted in grey, and remaining atoms are colored based on their local long-time correlation. Dark colors indicate that the normal inclination decorrelates, revealing dynamic regions. Bright colors highlight instead static regions over which the inclination hardly decorrelates. The snapshots (b-c) lie in the transition region, see Fig. 2(c), in which the defect arrangement gives rise to strong sample-to-sample fluctuations. The simulation box is indicated with dashed lines, and the scale bar drawn in (a) represents 5 nm.

insets in Fig. 2(b)). Our analysis thus focuses on extracting and comparing the long-time inclination correlation. Details are provided in the Methods section and in section S1.B of the SI, and its evolution with defect concentration is presented in Fig. 2(c).

For pristine graphene, the plateau value is $C_\theta(\tau \rightarrow \infty) \approx 0.8$. As the defect concentration increases, we observe a pattern mirroring that of the rms inclination, but even more striking. For very low concentrations, $C_\theta(\tau \rightarrow \infty)$ increases steadily but remains close to the pristine reference. Around a defect concentration of $\approx 0.1\%$, we observe a sudden jump, surpassing that seen in the static observable of Fig. 2(a). In addition, we observe a much larger variance across different spatial realisations. Beyond concentrations $\geq 0.15\%$, the plateau values increase steadily again with defect concentration. These results suggest a previously unreported disorder-driven dynamical transition from random thermal fluctuations ($C_\theta(\tau \rightarrow \infty) \approx 0.8$) to frozen ripples ($C_\theta(\tau \rightarrow \infty) \gtrsim 0.9$). Our conclusion is supported by our results reported in section S3.A.1 of the SI which demonstrate that the transition becomes sharper with increasing system size, suggesting a genuine dynamical transition in the macroscopic limit.

Our findings have important implications from multiple perspectives. First, the critical defect concentration observed in our study aligns quantitatively with the maximum of the non-monotonic behaviour of the Young's modulus,³⁸ suggesting a relationship between rippling dynamics and mechanical properties.³⁷ Second, the transition occurs at a concentration considerably lower than what is typically accessible in AIMD simulations, implying potential limitations in using first-principles methods to study transport properties in defective graphene. The dependence of rippling dynamics on the spatial arrangement of defects, however, poses an

intriguing possibility for locally engineering dynamics and, thus, properties of graphene by introducing defects. Understanding the nanoscale physical mechanisms involved in this process is crucial. To address this, we resolve the per-atom inclination correlation at long times for all studied systems. We show in Fig. 3 snapshots selected based on their global long-time correlation, see Fig. 2(c). Each atom is color-coded based on its atomic $C_\theta(\tau \rightarrow \infty)$. For a comprehensive overview of results and full computational details, the reader is referred to the section S1.B and S2.B of the SI.

The heatmaps reveal distinct local dynamics influenced by defect concentration and spatial arrangement. At dilute concentration, shown in Fig. 3(a), the influence of defects on the dynamics is already quite pronounced and fairly long-ranged, extending up to 1-2 nm away from the defect site. Beyond such short distances the dynamical influence of the defect is negligible at these lowest concentrations. This observation extends our previous findings,³⁴ where structural analysis suggested weak static interactions between divacancy defects at very low concentrations, to the dynamics. At higher concentrations, defect-defect interactions become stronger, giving rise to important local strains which lead to significantly restrained inclination dynamics. This includes dynamically frozen paths connecting defects separated by up to 10 nm, i.e. defects conspire to constrain the dynamics over scales far exceeding those observed at low defect concentration. Additionally, in contrast, we identify regions extending over a few nanometers which exhibit $C_\theta(\tau \rightarrow \infty)$ values lower than those of the pristine reference, indicating more dynamic and volatile behaviour. A careful investigation reveals that these areas undergo spontaneous mirror buckling events during which their curvature flips. Our work thus demonstrates that mirror buckling, detected experimentally at a global scale in a compressed pristine graphene

sheet,²⁵ can be induced at the nanoscale thanks to the insertion of atomic defects. In fact, these events already occur in systems around the critical defect concentration of 0.1%. This is further supported by our analysis of the mean-squared displacement (MSD) in section S3.B.2 of the SI. Indeed, we show that the long-time MSD at these intermediate concentrations exceeds that of pristine graphene. This is rationalised by that fact that the MSD is dominated by the atoms which lie in the regions subject to mirror-buckling events. This explains why the long-time MSD value can be larger than pristine graphene, which suggests more dynamic fluctuations, even though the average long-time inclination correlation is larger, suggesting a more constrained dynamics. All this indicates that with increasing defect concentration, the system initially becomes more mobile and flexible, at least locally, before eventually converging to a highly static pattern around which atoms fluctuate as more defects are introduced. The presence of such local mirror-buckling regions at intermediate densities could help explain the experimental observation of a non-monotonic Young’s modulus in defective graphene.³⁸

The most intriguing concentration range for nanoengineering lies around the transition concentration of 0.1%. In Fig. 3(b) and 3(c), identical defect densities with varying spatial arrangements result in significantly different $C_\theta(\tau \rightarrow \infty)$. This reveals that in this intermediate regime the dynamics depends on the precise positioning of the defects. In the more volatile system depicted in Fig. 3(b), the defects exhibit minimal interaction, resulting in a purely local impact. Consequently, in the defect-free areas, $C_\theta(\tau \rightarrow \infty)$ remains close to the pristine level. In contrast, the defects in the system shown in Fig. 3(c) strongly interact, leading to the formation of *frozen* pathways with $C_\theta(\tau \rightarrow \infty) \approx 1.0$. These pathways connect all defects across the sheet, inducing a long-range fixation effect on atoms beyond the close vicinity of the defects. These findings highlight the need for a systematic and comprehensive study of the high-dimensional interplay between defects, which would consider pairwise as well as many-body distances and orientations, to establish effective guidelines for the design of areas exhibiting the desired mobility. Importantly, this study represents the first instance where we can resolve and quantify the dynamics of defective graphene locally. Our results and methodology pave the way to designing the dynamics and gaining insight into arranging not only divacancies in graphene but any atomic defect, in any 2D material.

III. CONCLUSION

We have reported a large-scale machine learning-driven molecular dynamics study on the impact of divacancy defects at varying concentrations on the rippling dynamics in graphene. We introduce a novel approach based on the local inclination to quantify both corrugation and

time-dependent fluctuations, which can be compared to experimental electron diffraction patterns. We unveil a discontinuity in both static and dynamic measures at low defect concentrations of $\approx 0.1\%$ suggesting a disorder-driven dynamical transition from freely propagating ripples to frozen rippling dynamics. The precise location of this critical concentration, however, is likely to vary from one type of defect to another and also from one type of 2D material to the next. Exploring such sensitivities, as well as obtaining direct experimental confirmation of the predictions reported here, e.g. with ultrafast electron crystallography,²⁶ will make interesting work for the future. Nonetheless, the quantitative alignment of our predicted critical concentration with the peak in the non-monotonic Young’s modulus-defect density relationship³⁸ suggests a close interconnection between dynamics and mechanical properties. In addition, based on experimental results,⁵⁰ our work introduces the potential use of atomic defects to create nanoscale areas with significant curvature in graphene sheets, and in turn generate strong pseudomagnetic fields and unconventional electronic properties. On the theoretical side, future work based on discrete real space models and nonlinear continuum elastic models will be required to fully characterize the disorder-driven transition predicted here. In particular, past works^{51–53} on thin elastic sheets comprising ordered dilation impurities revealed interesting critical phenomena and physical behaviour. Extending these works to randomly positioned compression impurities, mimicking the divacancy defects, is of great interest. Our analysis of local membrane fluctuations provides initial mechanistic insights, highlighting the pivotal role of divacancy interactions in implementing pathways or areas of desired mobility.

Overall, our work attains an unprecedented atomic-level resolution of graphene dynamics, with findings readily applicable to the broad spectrum of 2D materials. This offers exciting prospects for the development of innovative devices, in which the behavior of ripples, motion of adsorbates, and the membrane’s catalytic activity are directly controlled through reflection and refraction at defects. Our work demonstrates the potential of employing atomic defects towards various applications and the possibility of tailored directional phonon-mediated flow in nanofluidics.

IV. METHODS

A. Molecular Dynamics Simulations

We study the impact of atomic defects on the rippling dynamics of free-standing graphene via molecular dynamics simulations. We use the machine learning-based Gaussian approximation potential⁵⁴ (GAP) for carbon, GAP-20.⁵⁵ This computational approach allows us to simulate with first principles accuracy large system sizes and timescales inaccessible to expensive *ab*

initio methods.^{56,57} This is necessary to account for spatially extended ripples⁷ and capture defect-defect interactions.^{58,59} Unlike simpler classical force fields for carbon, the GAP-20 potential has been shown to reliably predict a variety of properties of graphene, including its phonon dispersion spectrum, elastic constants, defect structure and formation energies,⁵⁵ and provides first principles quality even at high defect concentrations.³⁴ A detailed description of the GAP framework can be found elsewhere.^{54,60,61}

The pristine graphene samples are composed of 7200 carbon atoms. The defective ones are created starting from a perfectly flat and pristine graphene sheet, and iteratively removing two adjacent carbon atoms. The reconstruction of divacancy defects is not enforced in the initial configuration and occurs spontaneously during the simulation. We do not observe any defect migration. The position and orientation of the divacancies are chosen randomly, yet we ensure a minimum separation of 10 Å between defect centers. Following previous works,^{34,62} we define the defect concentration as the ratio of removed atoms to the total number of atoms in a pristine graphene sheet. We study defect concentrations from $\approx 0.03\%$ (corresponding to an isolated defect) to a high level of 1% (corresponding to 36 divacancy defects, or 7128 carbon atoms). We show representative snapshots of pristine and highly defective samples in Fig. 1. For each defect concentration, we run several simulations placing the divacancies at various positions and orientations.

The simulations were performed at 300 K and zero stress, with periodic boundary conditions, using the LAMMPS software package.⁶³ A detailed description of the simulation setup can be found in section S1.A of the SI. The entire post-processing analysis for all simulations was performed in Python using the ASE,⁶⁴ MDAnalysis,^{65,66} and OVITO⁶⁷ software packages. Computational details and additional convergence tests for both system size and simulation time are presented in sections S1.B and S3.A as well as S3.B of the SI, respectively.

B. Measuring Corrugation and Dynamics

We quantify the static corrugation of a graphene sheet based on the rms inclination which represents the average deviation of the surface normal from its mean (z) direction. For each atom, we compute the vector normal to the membrane by locally fitting the surface defined by neighboring carbon atoms (see section S1.B of the SI for details). The normal inclination θ , illustrated in Fig. 1(g), is defined as the angle between the normal vector and the z direction. This approach extends the concept of the pyramidalisation angle⁶⁸ beyond the nearest neighbors and allows for a smooth and accurate

representation of the local surface. Our method fully accounts for the corrugated nature of the membrane and allows a comparison with experimental efforts to measure graphene’s corrugation via TEM diffraction patterns.⁶

Notably, both experiments²² and computational work⁶⁹ suggest an exponential relationship, $\theta_{\text{rms}} \propto \exp(-l/L)$, where L is the size of the free-standing graphene sheet and the parameter l can be interpreted as the inverse resolution of the measurement. Specifically, l corresponds to the electron coherence length in TEM experiments, while in simulations, l measures the patch size over which the corrugation is averaged. In our approach, individually fitting the angle for each atom without any spatial averaging results in a basically infinite resolution of $l = 0$. This allows a direct comparison to electron diffraction experiments for graphene sheets of about 1 μm , where typical electron coherence lengths result in very low $l/L \leq 0.02$. For a more details discussion on this aspect, the reader is referred to section S3.A.1 of the SI.

To assess the dynamics of the graphene sheet, we compute the autocorrelation function of the normal inclination, normalised by its equal-time value, which we denote $C_\theta(\tau)$. This function tracks the variation of the surface normal over time, providing valuable insights into the system’s dynamic behaviour. To enable a straightforward comparison across systems, we fit an exponential function to $C_\theta(\tau)$ and extract the plateau value, denoted as $C_\theta(\tau \rightarrow \infty)$. Comprehensive details are provided in section S1.B of the SI.

SUPPLEMENTARY INFORMATION

See the Supporting Information for a detailed description of the molecular dynamics simulations (S1.A), the computation of the normal inclination and its autocorrelation function (S1.B), a comprehensive of our results for all systems (S2), an analysis of the dependence of our results on system size and simulation duration (S3.A), and comparison with alternative observables (S3.B). In addition, we provide videos of the temporal evolution over 1 ns of different graphene systems including the pristine reference as well as the four systems depicted in Figure 3.

ACKNOWLEDGEMENTS

We are grateful to the UK Materials and Molecular Modelling Hub for computational resources, which is partially funded by EPSRC (EP/P020194/1 and EP/T022213/1). Through our membership of the UK’s HEC Materials Chemistry Consortium, which is funded

by EPSRC (EP/L000202 and EP/R029431), this work used the ARCHER and ARCHER2 UK National Supercomputing Service (<http://www.archer2.ac.uk>). We are also grateful for the computational resources granted by the UCL Grace High Performance Computing Facility (Grace@UCL), and associated support services. A. M. acknowledges support from the European Union under the “n-AQUA” European Research Council project (Grant No. 101071937).

REFERENCES

- ¹N. D. Mermin, “Crystalline Order in Two Dimensions,” *Physical Review* **176**, 250–254 (1968).
- ²A. K. Geim and K. S. Novoselov, “The rise of graphene,” *Nature Mater* **6**, 183–191 (2007).
- ³C. Lee, X. Wei, J. W. Kysar, and J. Hone, “Measurement of the Elastic Properties and Intrinsic Strength of Monolayer Graphene,” *Science* **321**, 385–388 (2008).
- ⁴A. H. C. Neto, F. Guinea, N. M. R. Peres, K. S. Novoselov, and A. K. Geim, “The electronic properties of graphene,” *Rev. Mod. Phys.* **81**, 109–162 (2009), arXiv:0709.1163 [cond-mat].
- ⁵A. A. Balandin, “Thermal properties of graphene and nanostructured carbon materials,” *Nature Mater* **10**, 569–581 (2011).
- ⁶J. C. Meyer, A. K. Geim, M. I. Katsnelson, K. S. Novoselov, T. J. Booth, and S. Roth, “The structure of suspended graphene sheets,” *Nature* **446**, 60–63 (2007).
- ⁷A. Fasolino, J. Los, and M. I. Katsnelson, “Intrinsic ripples in graphene,” *Nature Materials* **6**, 858–861 (2007).
- ⁸A. Lobkovsky, S. Gentges, H. Li, and D. Morse, “Scaling Properties of Stretching Ridges in a Crumpled Elastic Sheet,” *Science* **270**, 1482–1485 (1995).
- ⁹J. Martin, N. Akerman, G. Ulbricht, T. Lohmann, J. H. Smet, K. Von Klitzing, and A. Yacoby, “Observation of electron–hole puddles in graphene using a scanning single-electron transistor,” *Nature Phys* **4**, 144–148 (2008).
- ¹⁰F. Guinea, M. I. Katsnelson, and M. A. Vozmediano, “Midgap states and charge inhomogeneities in corrugated graphene,” *Physical Review B - Condensed Matter and Materials Physics* **77**, 075422 (2008).
- ¹¹S. V. Morozov, K. S. Novoselov, M. I. Katsnelson, F. Schedin, L. A. Ponomarenko, D. Jiang, and A. K. Geim, “Strong Suppression of Weak Localization in Graphene,” *Phys. Rev. Lett.* **97**, 016801 (2006).
- ¹²D. C. Elias, R. R. Nair, T. M. G. Mohiuddin, S. V. Morozov, P. Blake, M. P. Halsall, A. C. Ferrari, D. W. Boukhvalov, M. I. Katsnelson, A. K. Geim, and K. S. Novoselov, “Control of Graphene’s Properties by Reversible Hydrogenation: Evidence for Graphane,” *Science* **323**, 610–613 (2009).
- ¹³D. W. Boukhvalov and M. I. Katsnelson, “Enhancement of chemical activity in corrugated graphene,” *Journal of Physical Chemistry C* **113**, 14176–14178 (2009).
- ¹⁴P. Z. Sun, W. Q. Xiong, A. Bera, I. Timokhin, Z. F. Wu, A. Mishchenko, M. C. Sellers, B. L. Liu, H. M. Cheng, E. Janzen, J. H. Edgar, I. V. Grigorieva, S. J. Yuan, and A. K. Geim, “Unexpected catalytic activity of nanorippled graphene,” *Proc. Natl. Acad. Sci. U.S.A.* **120**, e2300481120 (2023).
- ¹⁵M. Ma, G. Tocci, A. Michaelides, and G. Aeppli, “Fast diffusion of water nanodroplets on graphene,” *Nature Mater* **15**, 66–71 (2016).
- ¹⁶S. Marbach, D. S. Dean, and L. Bocquet, “Transport and dispersion across wiggling nanopores,” *Nature Phys* **14**, 1108–1113 (2018).
- ¹⁷C. H. Lui, L. Liu, K. F. Mak, G. W. Flynn, and T. F. Heinz, “Ultraflat graphene,” *Nature* **462**, 339–341 (2009).
- ¹⁸W. Bao, F. Miao, Z. Chen, H. Zhang, W. Jang, C. Dames, and C. N. Lau, “Controlled ripple texturing of suspended graphene and ultrathin graphite membranes,” *Nature Nanotechnology* **4**, 562–566 (2009).
- ¹⁹O. Lehtinen, S. Kurasch, A. V. Krasheninnikov, and U. Kaiser, “Atomic scale study of the life cycle of a dislocation in graphene from birth to annihilation,” *Nature Communications* **4**, 2098 (2013).
- ²⁰U. Ludacka, M. Monazam, C. Rentenberger, M. Friedrich, U. Stefanelli, J. Meyer, and J. Kotakoski, “In situ control of graphene ripples and strain in the electron microscope,” *npj 2D Materials and Applications* **2**, 25 (2018).
- ²¹F. L. Thiemann, P. Rowe, E. A. Müller, and A. Michaelides, “Machine Learning Potential for Hexagonal Boron Nitride Applied to Thermally and Mechanically Induced Rippling,” *The Journal of Physical Chemistry C* **124**, 22278–22290 (2020).
- ²²R. Singh, D. Scheinecker, U. Ludacka, and J. Kotakoski, “Corrugations in free-standing graphene,” *Nanomaterials* **12** (2022).
- ²³Y. Z. He, H. Li, P. C. Si, Y. F. Li, H. Q. Yu, X. Q. Zhang, F. Ding, K. M. Liew, and X. F. Liu, “Dynamic ripples in single layer graphene,” *Applied Physics Letters* **98**, 063101 (2011).
- ²⁴P. Xu, M. Neek-Amal, S. Barber, J. Scholz, M. Ackerman, P. Thibado, A. Sadeghi, and F. Peeters, “Unusual ultra-low-frequency fluctuations in freestanding graphene,” *Nature Communications* **5**, 3720 (2014).
- ²⁵M. L. Ackerman, P. Kumar, M. Neek-Amal, P. M. Thibado, F. M. Peeters, and S. Singh, “Anomalous dynamical behavior of free-standing graphene membranes,” *Physical Review Letters* **117**, 126801 (2016).
- ²⁶J. Hu, G. M. Vanacore, A. Cepellotti, N. Marzari, and A. H. Zewail, “Rippling ultrafast dynamics of suspended 2D monolayers, graphene,” *Proceedings of the National Academy of Sciences of the United States of America* **113**, E6555–E6561 (2016).
- ²⁷G. Pacchioni, “Graphene: Taming the ripples,” *Nat Rev Mater* **1**, 16090 (2016).
- ²⁸E. Granato, M. Greb, K. R. Elder, S. C. Ying, and T. Ala-Nissila, “Dynamic scaling of out-of-plane fluctuations in free-standing graphene,” *Physical Review B - Condensed Matter and Materials Physics* **105**, L201409 (2022).
- ²⁹E. Granato, K. R. Elder, S. C. Ying, and T. Ala-Nissila, “Dynamics of fluctuations and thermal buckling in graphene from a phase-field crystal model,” *Physical Review B - Condensed Matter and Materials Physics* **107**, 035428 (2023).
- ³⁰M. Neek-Amal, P. Xu, J. Scholz, M. Ackerman, S. Barber, P. Thibado, A. Sadeghi, and F. Peeters, “Thermal mirror buckling in freestanding graphene locally controlled by scanning tunneling microscopy,” *Nat Commun* **5**, 4962 (2014).
- ³¹O. V. Yazyev and S. G. Louie, “Topological defects in graphene: Dislocations and grain boundaries,” *Physical Review B - Condensed Matter and Materials Physics* **81**, 195420 (2010).
- ³²J. H. Warner, E. R. Margine, M. Mukai, A. W. Robertson, F. Giustino, and A. I. Kirkland, “Dislocation-Driven Deformations in Graphene,” *Science* **337**, 209–212 (2012).
- ³³C. Hofer, C. Kramberger, M. R. A. Monazam, C. Mangler, A. Mittelberger, G. Argentero, J. Kotakoski, and J. C. Meyer, “Revealing the 3d structure of graphene defects,” *2D Materials* **5**, 045029 (2018).
- ³⁴F. L. Thiemann, P. Rowe, A. Zen, E. A. Müller, and A. Michaelides, “Defect-Dependent Corrugation in Graphene,” *Nano Letters* **21**, 8143–8150 (2021).
- ³⁵G. López-Polín, M. Ortega, J. G. Vilhena, I. Alda, J. Gomez-Herrero, P. A. Serena, C. Gomez-Navarro, and R. Pérez, “Tailoring the thermal expansion of graphene via controlled defect creation,” *Carbon* **116**, 670–677 (2017).
- ³⁶A. Zandiatashbar, G. H. Lee, S. J. An, S. Lee, N. Mathew, M. Terrones, T. Hayashi, C. R. Picu, J. Hone, and N. Koratkar, “Effect of defects on the intrinsic strength and stiffness of graphene,” *Nature Communications* **5**, 3186 (2014).
- ³⁷R. J. Nicholl, H. J. Conley, N. V. Lavrik, I. Vlassiok, Y. S. Puzrev, V. P. Sreenivas, S. T. Pantelides, and K. I. Bolotin, “The effect of intrinsic crumpling on the mechanics of free-standing graphene,” *Nature Communications* **6**, 8789 (2015).

- ³⁸G. López-Polín, C. Gómez-Navarro, V. Parente, F. Guinea, M. I. Katsnelson, F. Pérez-Murano, and J. Gómez-Herrero, “Increasing the elastic modulus of graphene by controlled defect creation,” *Nature Physics* **11**, 26–31 (2014).
- ³⁹G. Lopez-Polin, C. Gomez-Navarro, and J. Gomez-Herrero, “The effect of rippling on the mechanical properties of graphene,” *Nano Materials Science* **4**, 18–26 (2022).
- ⁴⁰K. Anggara, H. Ochner, S. Szilagyi, L. Malavolti, S. Rauschenbach, and K. Kern, “Landing Proteins on Graphene Trampoline Preserves Their Gas-Phase Folding on the Surface,” *ACS Cent. Sci.* **9**, 151–158 (2023).
- ⁴¹W. B. L. Gao Yang, Lihua Li and M. C. Ng, “Structure of graphene and its disorders: a review,” *Science and Technology of Advanced Materials* **19**, 613–648 (2018).
- ⁴²A. V. Krasheninnikov and F. Banhart, “Engineering of nanostructured carbon materials with electron or ion beams,” *Nature Materials* **6**, 723–733 (2007).
- ⁴³A. W. Robertson, C. S. Allen, Y. A. Wu, K. He, J. Olivier, J. Neethling, A. I. Kirkland, and J. H. Warner, “Spatial control of defect creation in graphene at the nanoscale,” *Nature Communications* **3**, 1144 (2012).
- ⁴⁴T. Susi, J. C. Meyer, and J. Kotakoski, “Manipulating low-dimensional materials down to the level of single atoms with electron irradiation,” *Ultramicroscopy* **180**, 163–172 (2017).
- ⁴⁵X. Zhao, J. Kotakoski, J. C. Meyer, E. Sutter, P. Sutter, A. V. Krasheninnikov, U. Kaiser, and W. Zhou, “Engineering and modifying two-dimensional materials by electron beams,” *MRS Bulletin* **42**, 667–676 (2017).
- ⁴⁶F. Banhart, J. Kotakoski, and A. V. Krasheninnikov, “Structural defects in graphene,” *ACS Nano* **5**, 26–41 (2011).
- ⁴⁷J. Kotakoski, A. V. Krasheninnikov, U. Kaiser, and J. C. Meyer, “From point defects in graphene to two-dimensional amorphous carbon,” *Physical Review Letters* **106**, 105505 (2011).
- ⁴⁸A. J. Stone and D. J. Wales, “Theoretical studies of icosahedral C₆₀ and some related species,” *Chemical Physics Letters* **128**, 501–503 (1986).
- ⁴⁹Y. Liao, Z. Li, L. Chen, A. B. Croll, and W. Xia, “Crumpling Defective Graphene Sheets,” *Nano Letters* **23**, 3637–3644 (2023).
- ⁵⁰N. Levy, S. A. Burke, K. L. Meaker, M. Panlasigui, A. Zettl, F. Guinea, A. H. C. Neto, and M. F. Crommie, “Strain-induced pseudo-magnetic fields greater than 300 tesla in graphene nanobubbles,” *Science* **329**, 544–547 (2010).
- ⁵¹A. Plummer and D. R. Nelson, “Buckling and metastability in membranes with dilation arrays,” *Phys. Rev. E* **102**, 033002 (2020).
- ⁵²P. Z. Hanakata, A. Plummer, and D. R. Nelson, “Anomalous thermal expansion in ising-like puckered sheets,” *Phys. Rev. Lett.* **128**, 075902 (2022).
- ⁵³A. Plummer, P. Z. Hanakata, and D. R. Nelson, “Curvature as an external field in mechanical antiferromagnets,” *Phys. Rev. Mater.* **6**, 115203 (2022).
- ⁵⁴A. P. Bartók, M. C. Payne, R. Kondor, and G. Csányi, “Gaussian approximation potentials: The accuracy of quantum mechanics, without the electrons,” *Physical Review Letters* **104**, 136403 (2010).
- ⁵⁵P. Rowe, V. L. Deringer, P. Gasparotto, G. Csányi, and A. Michaelides, “An accurate and transferable machine learning potential for carbon,” *Journal of Chemical Physics* **153**, 034702 (2020).
- ⁵⁶J. Behler, “Perspective : Machine learning potentials for atomistic simulations,” *Journal of Chemical Physics* **145**, 170901 (2016).
- ⁵⁷V. L. Deringer, M. A. Caro, and G. Csányi, “Machine Learning Interatomic Potentials as Emerging Tools for Materials Science,” *Advanced Materials* **31**, 1902765 (2019).
- ⁵⁸G. G. Samsonidze, G. G. Samsonidze, and B. I. Yakobson, “Energetics of Stone-Wales defects in deformations of monoatomic hexagonal layers,” *Computational Materials Science* **23**, 62–72 (2002).
- ⁵⁹S. K. Jain, G. T. Barkema, N. Mousseau, C. M. Fang, and M. A. Van Huis, “Strong Long-Range Relaxations of Structural Defects in Graphene Simulated Using a New Semiempirical Potential,” *Journal of Physical Chemistry C* **119**, 9646–9655 (2015).
- ⁶⁰A. P. Bartók and G. Csányi, “Gaussian approximation potentials: A brief tutorial introduction,” *International Journal of Quantum Chemistry* **115**, 1051–1057 (2015).
- ⁶¹V. L. Deringer, A. P. Bartók, N. Bernstein, D. M. Wilkins, M. Ceriotti, and G. Csányi, “Gaussian Process Regression for Materials and Molecules,” *Chemical Reviews* **121**, 10073–10141 (2021).
- ⁶²B. Mortazavi and S. Ahzi, “Thermal conductivity and tensile response of defective graphene: A molecular dynamics study,” *Carbon* **63**, 460–470 (2013).
- ⁶³S. Plimpton, “Fast Parallel Algorithms for Short-Range Molecular Dynamics,” *Journal of Computational Physics* **117**, 1–19 (1995).
- ⁶⁴A. Hjorth Larsen, J. Jørgen Mortensen, J. Blomqvist, I. E. Castelli, R. Christensen, M. Dułak, J. Friis, M. N. Groves, B. Hammer, C. Hargus, E. D. Hermes, P. C. Jennings, P. Bjerre Jensen, J. Kermode, J. R. Kitchin, E. Leonhard Kolsbjerg, J. Kubal, K. Kaasbjerg, S. Lysgaard, J. Bergmann Maronsson, T. Maxson, T. Olsen, L. Pastewka, A. Peterson, C. Rostgaard, J. Schiøtz, O. Schütt, M. Strange, K. S. Thygesen, T. Vegge, L. Vilhelmsen, M. Walter, Z. Zeng, and K. W. Jacobsen, “The atomic simulation environment - A Python library for working with atoms,” *Journal of Physics Condensed Matter* **29**, 273002 (2017).
- ⁶⁵N. Michaud-Agrawal, E. J. Denning, T. B. Woolf, and O. Beckstein, “Software News and Updates MDAnalysis: A Toolkit for the Analysis of Molecular Dynamics Simulations,” *Journal of Computational Chemistry* **32**, 2319–2327 (2011).
- ⁶⁶R. Gowers, M. Linke, J. Barnoud, T. Reddy, M. Melo, S. Seyler, J. Domański, D. Dotson, S. Buchoux, I. Kenney, and O. Beckstein, “MDAnalysis: A Python Package for the Rapid Analysis of Molecular Dynamics Simulations,” *Proceedings of the 15th Python in Science Conference*, 98–105 (2016).
- ⁶⁷A. Stukowski, “Visualization and analysis of atomistic simulation data with OVITO—the Open Visualization Tool,” *Modelling and Simulation in Materials Science and Engineering* **18**, 015012 (2010).
- ⁶⁸R. C. Haddon, “Chemistry of the fullerenes: The manifestation of strain in a class of continuous aromatic molecules,” *Science* **261**, 1545–1550 (1993).
- ⁶⁹A. K. Singh and R. G. Hennig, “Scaling relation for thermal ripples in single and multilayer graphene,” *Physical Review B - Condensed Matter and Materials Physics* **87**, 094112 (2013).

Supporting information for: Defects induce phase transition from dynamic to static rippling in graphene

Fabian L. Thiemann,^{1,2, a)} Camille Scalliet,³ Erich A. Müller,⁴ and Angelos Michaelides^{2, b)}

¹⁾ IBM Research Europe, Keckwick Lane, Daresbury, WA4 4AD, United Kingdom

²⁾ Yusuf Hamied Department of Chemistry, University of Cambridge, Lensfield Road, Cambridge, CB2 1EW, United Kingdom

³⁾ Laboratoire de Physique de l'Ecole Normale Supérieure, ENS, Université PSL, CNRS, Sorbonne Université, Université de Paris, F-75005 Paris, France

⁴⁾ Department of Chemical Engineering, Sargent Centre for Process Systems Engineering, Imperial College London, South Kensington Campus, London SW7 2AZ, United Kingdom

(Dated: June 10, 2024)

In this supplementary information, we provide additional details on certain aspects of the study reported in the manuscript. This includes a detailed summary of the computational details and methods as well as an analysis of the sensitivity of the results.

S1 COMPUTATIONAL DETAILS

S1.A Molecular dynamics simulation

For all our classical molecular dynamics (MD) simulations, we employed monoclinic simulation cells where the length of the in-plane lattice vectors was ≈ 14.6 nm. Periodic boundary conditions were applied in all three directions. We ensured the graphene sheet did not interact with its periodic images perpendicular to the surface by adding a 5 nm vacuum, significantly surpassing the cutoff of the GAP-20 (1 nm).¹ The number of atoms varied with the number of defects introduced. While the pristine graphene sheet comprised 7200 atoms, systems of the highest defect concentration investigated (1.0% corresponding to 36 divacancy defects) comprised contained 7128 atoms. For all defective systems, the defects were distributed randomly with random orientations across the sheet while satisfying a minimum distance criterion of 1 nm between the defect centers. To sample the impact of different realisations of a respective defect concentration in the transition region, we went beyond the suggested 3 samples² and simulated 5 different spatial arrangements for systems comprising between 3 and 8 divacancy defects corresponding to defect concentrations between $\approx 0.083\%$ and $\approx 0.22\%$. For the remaining systems with 1, 2, 12, 20, and 36 defects two realisations of the respective defect density were performed. This was considered sufficient due to the small differences in the properties of interest between independent systems of these defect densities.

All simulations were performed with a timestep of 1 fs at a temperature of 300 K and zero strain in the isobaric-isothermal ensemble (NPT). The target temperature and stress were ensured by employing a Nosé-Hoover chain thermostat and barostat where the barostat was only applied to the in-plane dimensions. These were coupled to each other to guarantee that graphene retains its hexagonal nature. The interaction between carbon atoms was described using the GAP-20¹ which has been benchmarked in previous work² for graphene with a high density of divacancies achieving a maximum root mean square force error of ≈ 112.5 meV/Å with respect to its *ab initio* reference for defect concentrations of 3.0%. However, for the concentrations investigated in this work, a force error of ≈ 74.4 meV/Å was found. A thorough benchmarking of the potential with respect to the phonon dispersion curves and defect formation energies can be found in the original reference.¹ All simulations were started from a perfectly flat sheet ($z = 0$ for all atoms) and each system was equilibrated for 50 ps. Statistics were then gathered over a minimum of 850 ps, however, production runs for most systems were at least of the length of 1 ns and up to 1.6 ns. In section S3 S3.A S3.A.2, we show that the properties reported in the manuscript are in fact well converged for these simulation times. The atomic positions were saved every 100 fs. All simulations reported in the manuscript were performed using LAMMPS.³

^{a)}Electronic mail: fabian.thiemann@ibm.com

^{b)}Electronic mail: am452@cam.ac.uk

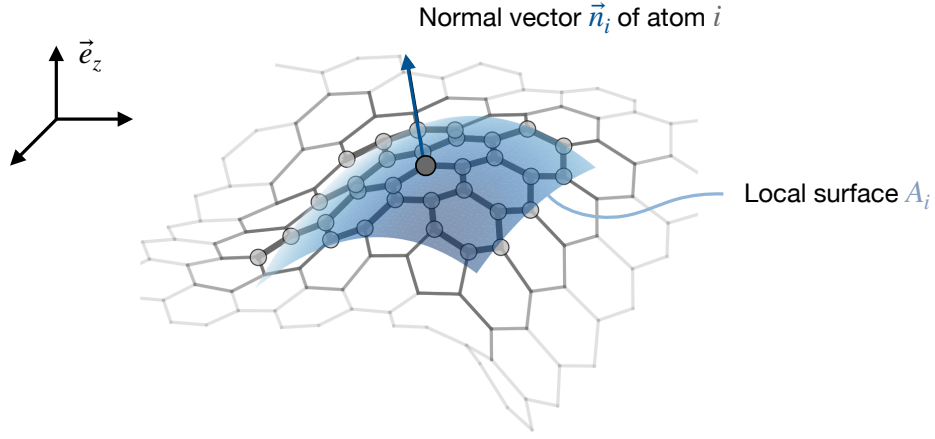


Figure S1. Schematic illustration of the atomic normal vector, \vec{n}_i , and the local surface, A_i , for an arbitrary atom i in graphene. The atoms highlighted by the spheres are used to fit the coefficients of the polynomial to approximate A_i .

S1.B Computation of observables

S1.B.1 Atomic normal vector

The atomic normal vector is the central quantity of this work and provides valuable information about the corrugation and dynamics of the system. Here we provide a comprehensive overview of the definition and computation of this measure. The atomic normal vector, denoted as \vec{n}_i , represents the vector perpendicular to local surface, A_i , of the graphene sheet, anchored at atom i . A schematic illustration of these quantities is shown in figure S1. To compute \vec{n}_i , we approximate the local surface, A_i , following an identical approach as in previous work.² Specifically, we identify all atoms within a distance of 4.5 Å from atom i and express the coordinates of these neighboring atoms relative to atom i . The value 4.5 Å corresponds to the cutoff of the many-body SOAP (smooth overlap of atomic positions) descriptor used by GAP-20.¹ While each atom's local environment in pristine graphene comprised 22 atoms, this number was slightly reduced for atoms in proximity to divacancies in defective systems. We then fit a two-dimensional second-order polynomial

$$z(x, y) = a + bx + cy + dxy + ex^2 + fy^2, \quad (1)$$

to the relative heights of these atoms to determine the local surface. For all atoms and frames in all systems the R^2 score of the fit exceeded 0.9 indicating an accurate description of the local surface A_i . We obtain the atomic normal vector \vec{n}_i by taking the gradient of the surface equation 1 at (0,0,0) i.e., at atom i ,

$$\vec{n}_i = [-b, -c, 1]^T. \quad (2)$$

S1.B.2 Atomic normal angle

The atomic normal angle, θ_i , is defined as the angle between the atomic normal vector \vec{n}_i , as defined in equation 2, and the unit vector in z-direction $\vec{e}_z = [0, 0, 1]^T$,

$$\cos \theta_i = \frac{\vec{n}_i \cdot \vec{e}_z}{\|\vec{n}_i\| \|\vec{e}_z\|}, \quad (3)$$

where the numerator corresponds to the dot product of the two vectors while the denominator is the product of their norms. Equation 3 further simplifies to

$$\theta_i = \arccos \left(\frac{1}{\sqrt{b^2 + c^2 + 1}} \right), \quad (4)$$

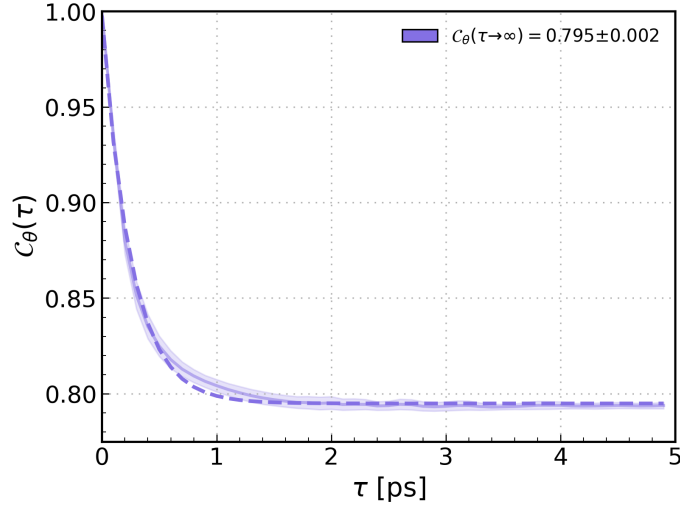


Figure S2. Angle autocorrelation function, $C_\theta(\tau)$, for pristine graphene. The continuous line corresponds to the values measured in our simulations, while the shaded area represents the threefold standard deviation estimated via bootstrapping. The dashed line corresponds to the fitted exponential function in equation 8 and in the legend we report the estimated plateau value based on this fit.

and only depends on the coefficients b and c of the local surface approximation function. The root mean square (rms) normal angle, which we refer to as rms inclination in the manuscript in line with reference,⁴ of the system can then be computed from the ensemble average

$$\theta_{\text{rms}} = \sqrt{\langle \theta^2 \rangle} = \left(\frac{1}{N_a N_f} \sum_{i=1}^{N_a} \sum_{j=1}^{N_f} \theta_i^2(t_j) \right)^{\frac{1}{2}}, \quad (5)$$

where N_a and N_f are the number of atoms and frames, respectively, and $\theta_i(t_j)$ is the atomic normal angle at atom i measured at frame j , or equivalently time t_j . To quantify the uncertainty associated with our measured value θ_{rms} for a given system, we calculate the standard deviation based on bootstrapping. This involves dividing each trajectory into four blocks and performing 10,000 resampling iterations. The error bars presented in the manuscript are, unless stated otherwise, derived from a threefold standard deviation obtained via this method.

S1.B.3 Angle autocorrelation function

To explore the impact of defects on the dynamics of atomic fluctuations in graphene, we extend the analysis to include time-dependent information on the atomic normal angle defined in equation 4. Specifically, we focus on the angle autocorrelation function, $\Phi_\theta(\tau)$, defined as

$$\Phi_\theta(\tau) = \langle \theta(\tau)\theta(0) \rangle = \frac{1}{N_a N_f} \sum_i^{N_a} \sum_j^{N_f} (\theta_i(t_j + \tau)\theta_i(t_j)), \quad (6)$$

where $\theta_i(t_j)$ is the atomic normal angle at atom i measured at time t_j , τ is the time lag, and the brackets $\langle \dots \rangle$ correspond to an ensemble average. The angle autocorrelation function is related to the rms inclination via $\Phi_\theta(\tau = 0) = \langle \theta^2 \rangle = \theta_{\text{rms}}^2$. We normalise the angle autocorrelation by the mean squared atomic angle to compare across different defect concentrations, defining the normalized angle autocorrelation function, $\mathcal{C}_\theta(\tau)$, as

$$\mathcal{C}_\theta(\tau) = \frac{\Phi_\theta(\tau)}{\Phi_\theta(0)} = \frac{\langle \theta(\tau)\theta(0) \rangle}{\langle \theta(0)\theta(0) \rangle} = \frac{\langle \theta(\tau)\theta(0) \rangle}{\langle \theta^2 \rangle}. \quad (7)$$

We compute it for time lags up to 5 ps which ensures the convergence of $\mathcal{C}_\theta(\tau)$ to a plateau value as shown in figure S2 for pristine graphene. We provide a comprehensive overview of the results for all systems in section S2 S2.A. To

accurately determine the plateau value of $\mathcal{C}_\theta(\tau)$, we fit it with an exponential decay

$$f(\tau) = A \exp(-k\tau) + c \quad (8)$$

and analyse its behaviour as τ approaches infinity ($f(\tau \rightarrow \infty) = c$). Across all systems discussed in the manuscript, we achieve R^2 scores above 0.98. The standard deviation for $\mathcal{C}_\theta(\tau)$ at any τ , as well as the estimate for plateau value $f(\tau \rightarrow \infty)$, was computed using the same bootstrapping approach described for the rms normal angle. While the ensemble average of the angle autocorrelation function in equation 6 provides the global perspective, computing $\mathcal{C}_\theta(\tau)$ separately for each individual atom allows to gain mechanistic insights, as demonstrated in Figure 3 of the manuscript. However, these atomwise calculations inherently rely on less converged statistics. Consequently, relatively low R^2 scores are obtained for some atoms in certain systems, leading to relatively high standard deviations. A full overview of these metrics is given in section S2 S2.B.

S2 COMPREHENSIVE OVERVIEW OF RESULTS

In this section, we present a comprehensive summary of all results and the corresponding estimated uncertainties discussed in the manuscript.

S2.A Angle autocorrelation function

Here, we report the angle autocorrelation function along with their plateau value $\mathcal{C}_\theta(\tau \rightarrow \infty)$ for all systems investigated. The pristine reference case is illustrated above in figure S2, while defective systems with fewer than 8 divacancy defects (corresponding to a concentration of $\approx 0.22\%$) are shown in figure S3. Conversely, angle autocorrelation functions for higher concentrations are depicted in Figure S4. For the sake of clarity, rather than plotting the fitted exponential function for each system, we merely highlight the plateau value estimated by the constant c in each plot.

S2.B Atomic heat maps based on plateau value of angle autocorrelation function

Shifting our focus from a global perspective to a local examination, we now transition from the ensemble average of the autocorrelation function to the atomwise calculation of the plateau value $\mathcal{C}_\theta(\tau)$. To assess the impact of less converged statistics on the results, we present accuracy metrics in table S1 for the fit of the exponential function to the atomic autocorrelation functions. Specifically, for each system, we provide the lowest R^2 value across all atoms and the count of atoms with an R^2 lower than a threshold of 0.8. In general, we observe better convergence in systems with lower defect concentrations, where the R^2 scores exhibit a monotonically decreasing trend with the number of defects. For systems with four or fewer divacancy defects, equivalent to a concentration of approximately 0.111 %, we obtain R^2 scores above the 0.8 threshold for all atoms. In more defective sheets, conversely, we find a substantial number of atoms with R^2 below 0.8. Still, we note that for most systems less than 1 % of particles fail to meet the convergence criterion. Only in systems with 20 defects or more (concentrations $\geq 0.556\%$) do we observe up to ≈ 11 % of atoms below our R^2 threshold of 0.8. We believe this does not compromise our ability to make qualitative statements about the results and overall behavior of these highly defective systems.

We show the atom-resolved plateau values of the angle autocorrelation function, $\mathcal{C}_\theta(\tau \rightarrow \infty)$, and the associated errors for all systems investigated in this work in the figures S5 to S11. In line with the analysis of the R^2 scores, we note a rise in uncertainty with higher defect concentrations. Interestingly, we also find significant deviations in the uncertainty across different spatial realisations of a given defect density as for example for 5 or 8 divacancy defects shown in the figures S8 and S10, respectively. Despite these variations, errors remain minimal for the majority of atoms, allowing for qualitative insights into local dynamics.

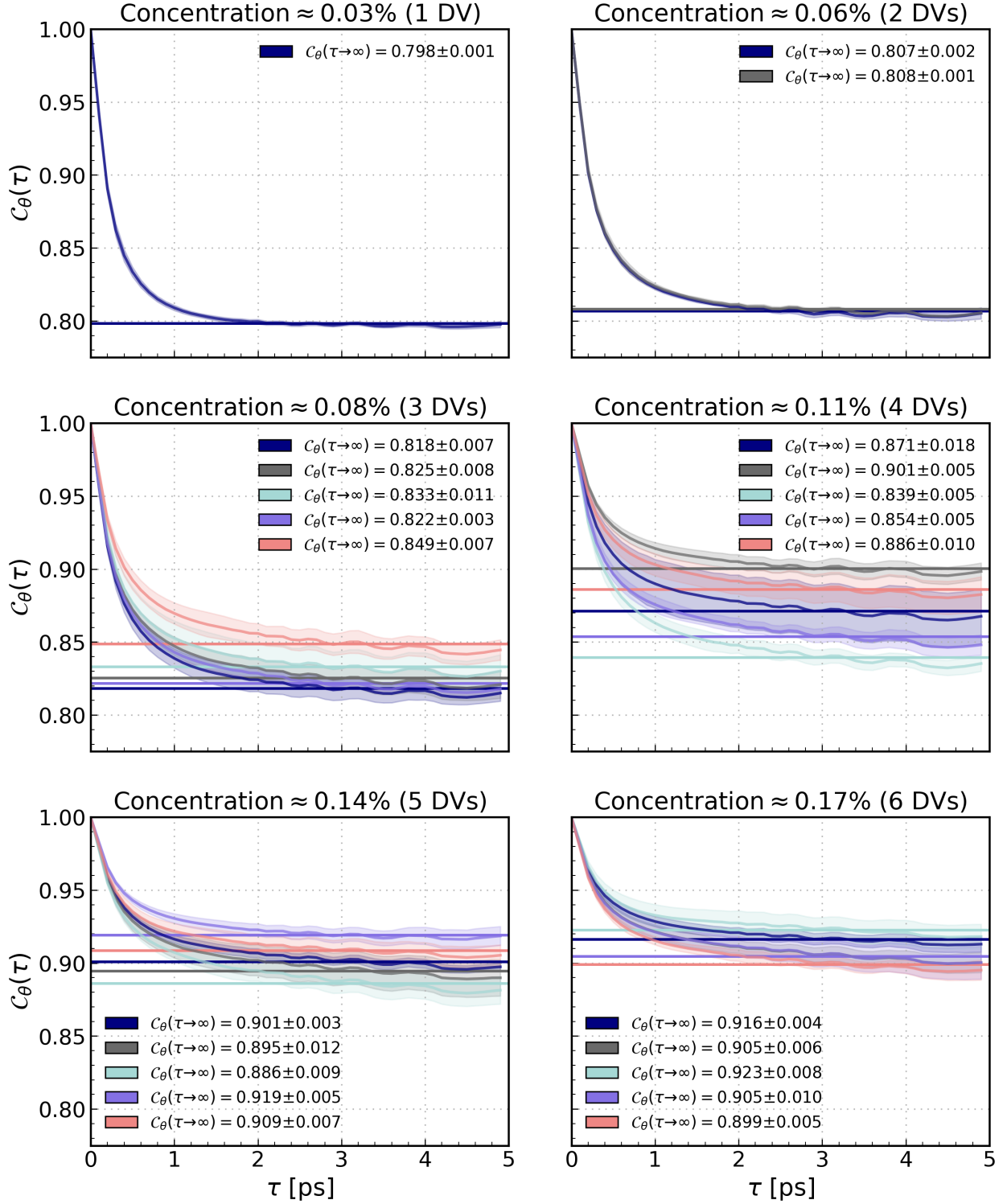


Figure S3. Angle autocorrelation function, $C_\theta(\tau)$, for systems comprising 1 to 6 divacancy defects corresponding to defect concentrations between $\approx 0.03\%$ and $\approx 0.17\%$. Each subplot illustrates between 1 and 5 systems of identical defect concentration but arranged in various spatial arrangements. The continuous line corresponds to the values measured in our simulations, while the shaded area represents the threefold standard deviation estimated via bootstrapping. The plateau value approximated by the constant c of the exponential function is illustrated by the horizontal line. For each system, the corresponding plateau values with their associated uncertainty are given in the legend.

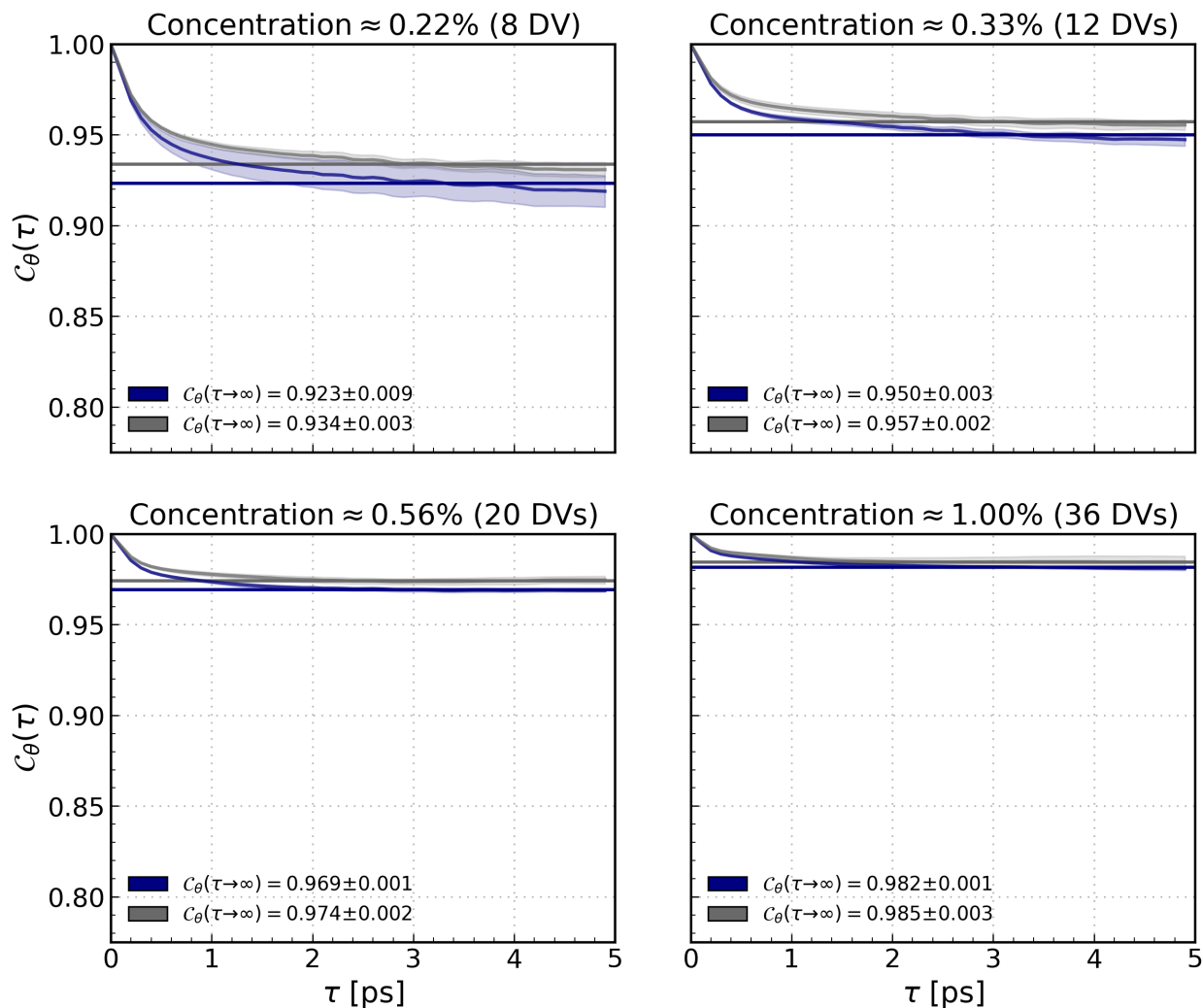


Figure S4. Angle autocorrelation function, $C_\theta(\tau)$, for systems comprising 8 to 36 divacancy defects corresponding to defect concentrations between $\approx 0.22\%$ and 1.00% . Each subplot illustrates 2 systems of identical defect concentration but arranged in various spatial arrangements. The continuous line corresponds to the values measured in our simulations, while the shaded area represents the threefold standard deviation estimated via bootstrapping. The plateau value approximated by the constant c of the exponential function is illustrated by the horizontal line. For each system, the corresponding plateau values with their associated uncertainty are given in the legend.

Table S1. Accuracy and convergence metrics related to the calculation of an atom-resolved $\mathcal{C}_\theta(\tau \rightarrow \infty)$ for each system.

System	Concentration [%]	Lowest R^2 score	#Atoms with $R^2 < 0.8$
Pristine	0.000	0.971	0
DV1 1	≈ 0.028	0.955	0
DV2 1	≈ 0.056	0.945	0
DV2 2		0.946	0
DV3 1	≈ 0.083	0.934	0
DV3 2		0.924	0
DV3 3		0.917	0
DV3 4		0.921	0
DV3 5		0.867	0
DV4 1	≈ 0.111	0.809	0
DV4 2		0.803	0
DV4 3		0.892	0
DV4 4		0.844	0
DV4 5		0.835	0
DV5 1	≈ 0.139	0.650	48
DV5 2		0.803	0
DV5 3		0.792	2
DV5 4		0.706	30
DV5 5		0.763	10
DV6 1	≈ 0.167	0.754	5
DV6 2		0.808	0
DV6 3		0.808	0
DV6 4		0.770	7
DV6 5		0.738	16
DV8 1	≈ 0.222	0.700	9
DV8 2		0.771	5
DV12 1	≈ 0.333	0.714	62
DV12 2		0.728	31
DV20 1	≈ 0.556	0.537	173
DV20 2		0.624	159
DV36 1	1.000	0.562	528
DV36 2		0.525	785

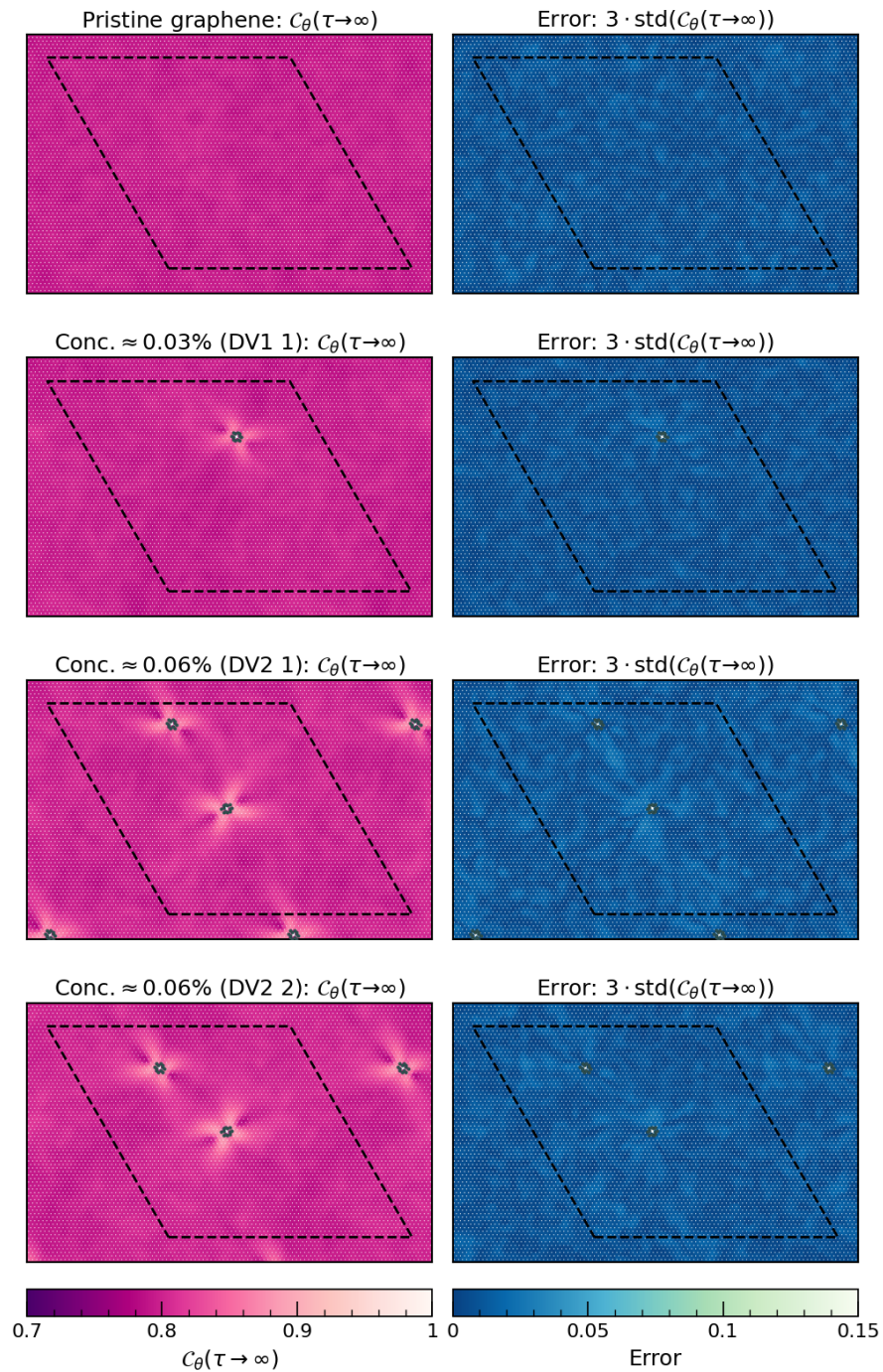


Figure S5. Atom-resolved plateau values of the angle autocorrelation function, $C_\theta(\tau \rightarrow \infty)$, for systems comprising up to 2 divacancy defects corresponding to a defect concentration of up to $\approx 0.06\%$. The atoms forming a divacancy are highlighted in grey. For each system we report the calculated atomic values (left) as well as the associated error based on the threefold standard deviation estimated via bootstrapping (right).

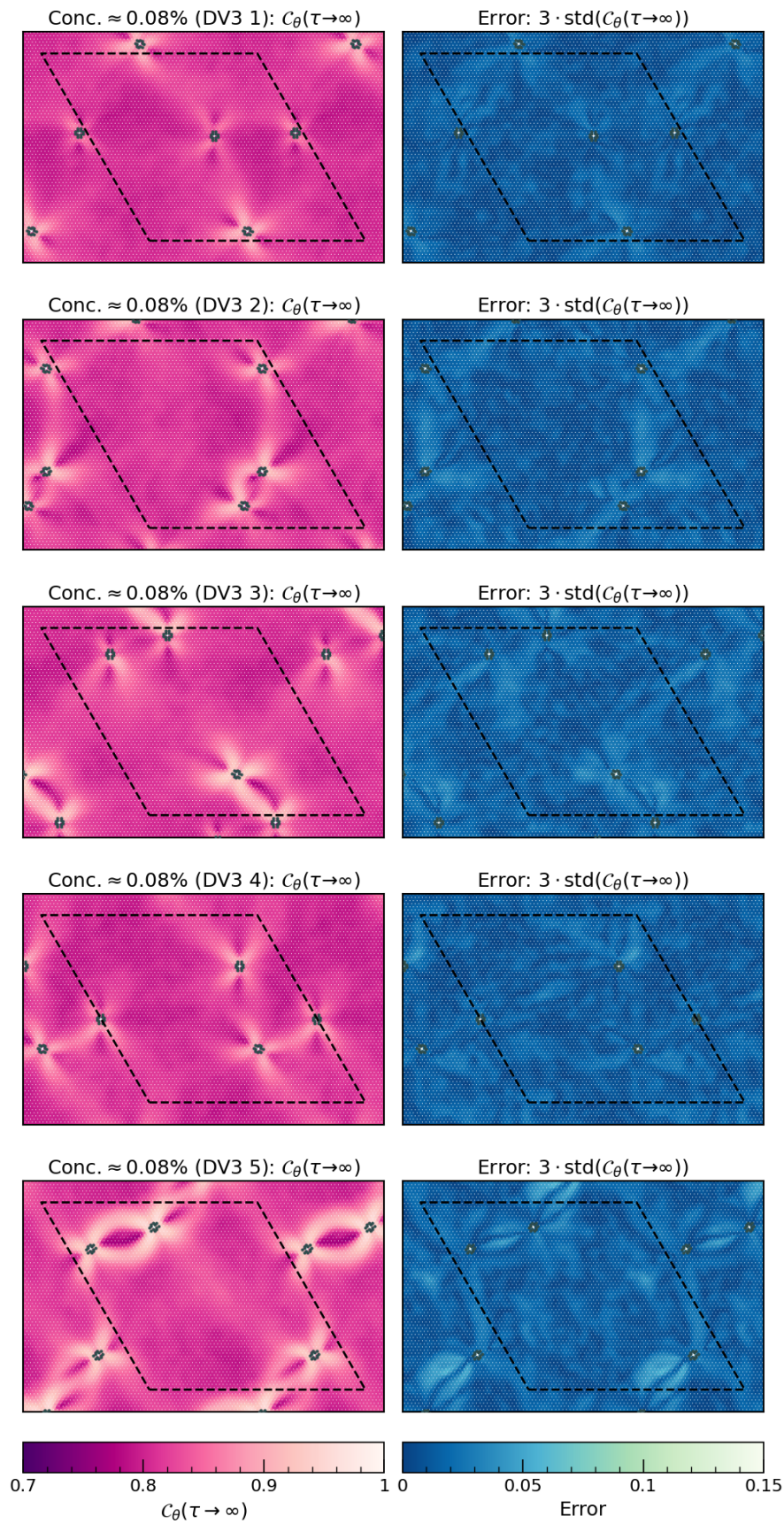


Figure S6. Atom-resolved plateau values of the angle autocorrelation function, $C_\theta(\tau \rightarrow \infty)$, for systems comprising 3 divacancy defects corresponding to a defect concentration of $\approx 0.08\%$. The atoms forming a divacancy are highlighted in grey. For each system we report the calculated atomic values (left) as well as the associated error based on the threefold standard deviation estimated via bootstrapping (right).

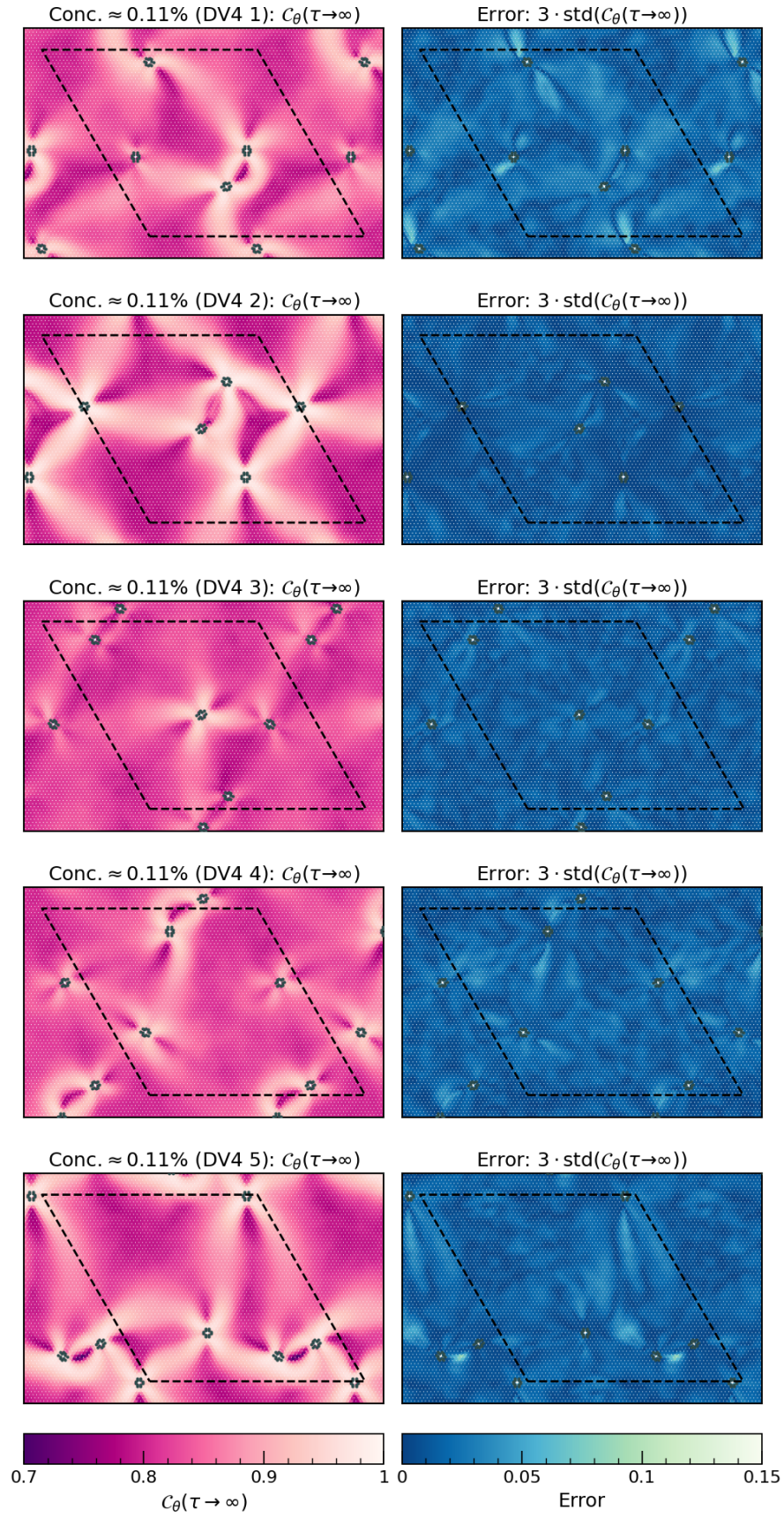


Figure S7. Atom-resolved plateau values of the angle autocorrelation function, $C_\theta(\tau \rightarrow \infty)$, for systems comprising 4 divacancy defects corresponding to a defect concentration of $\approx 0.11\%$. The atoms forming a divacancy are highlighted in grey. For each system we report the calculated atomic values (left) as well as the associated error based on the threefold standard deviation estimated via bootstrapping (right).

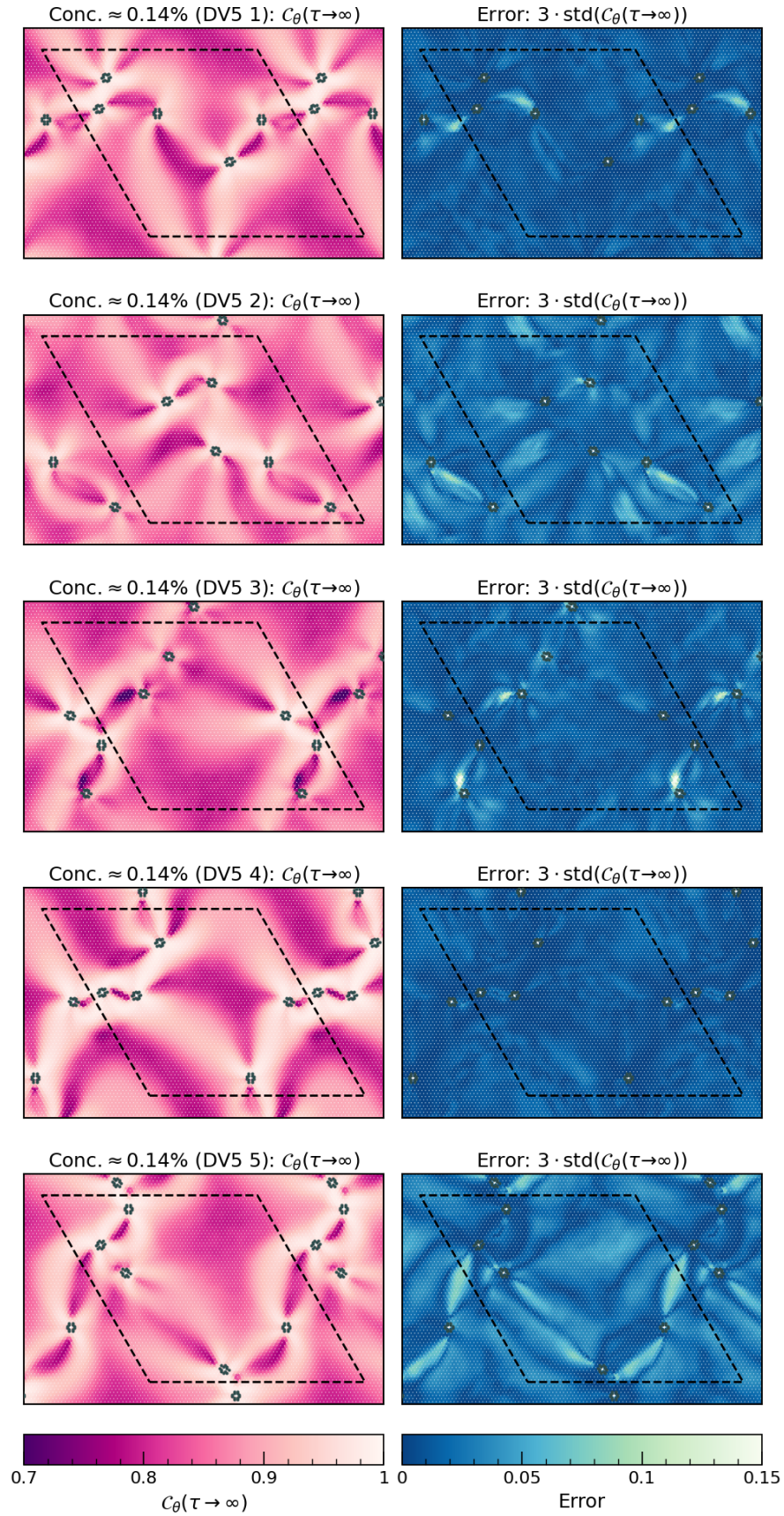


Figure S8. Atom-resolved plateau values of the angle autocorrelation function, $C_\theta(\tau \rightarrow \infty)$, for systems comprising 5 divacancy defects corresponding to a defect concentration of $\approx 0.14\%$. The atoms forming a divacancy are highlighted in grey. For each system we report the calculated atomic values (left) as well as the associated error based on the threefold standard deviation estimated via bootstrapping (right).

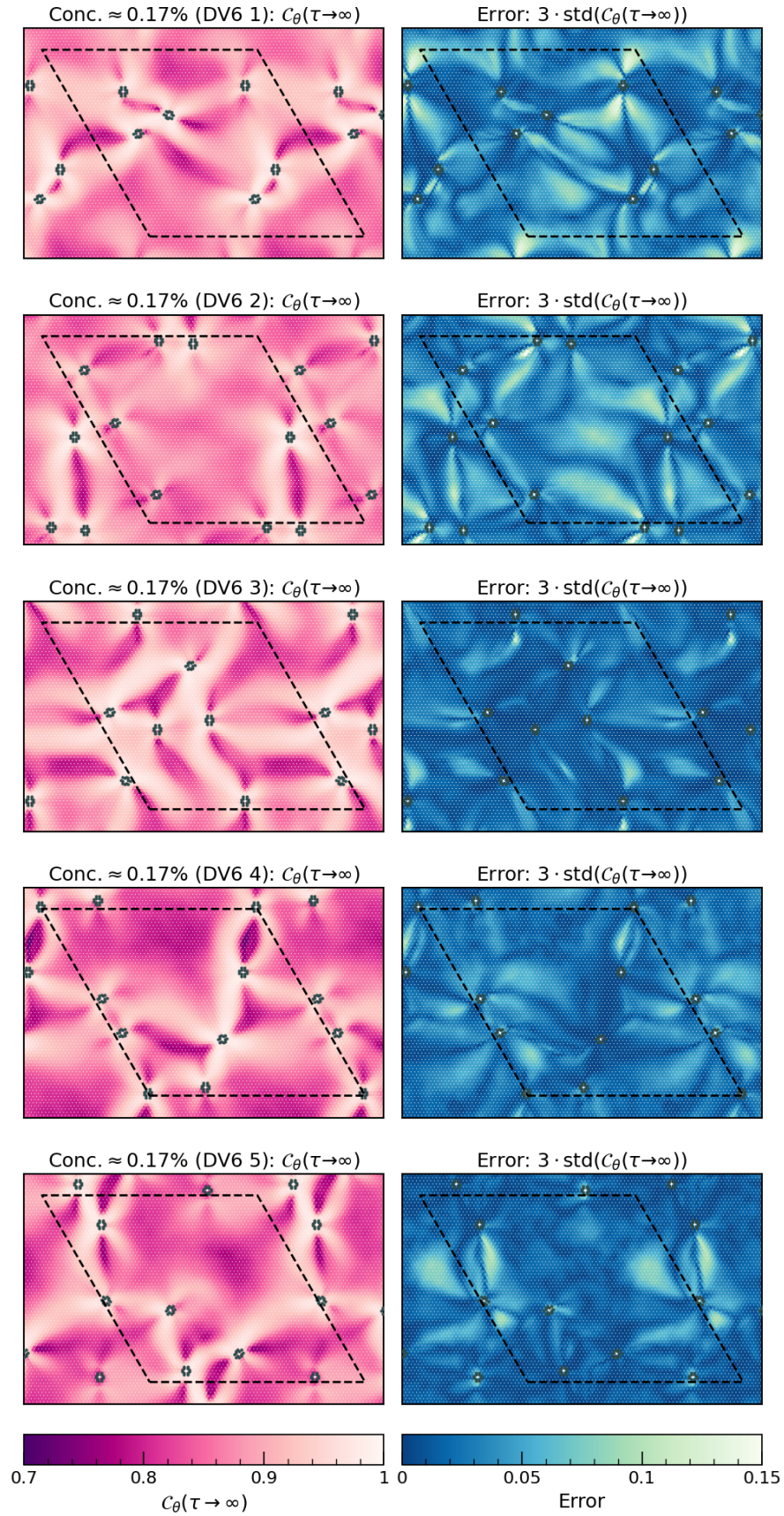


Figure S9. Atom-resolved plateau values of the angle autocorrelation function, $C_\theta(\tau \rightarrow \infty)$, for systems comprising 6 divacancy defects corresponding to a defect concentration of $\approx 0.17\%$. The atoms forming a divacancy are highlighted in grey. For each system we report the calculated atomic values (left) as well as the associated error based on the threefold standard deviation estimated via bootstrapping (right).

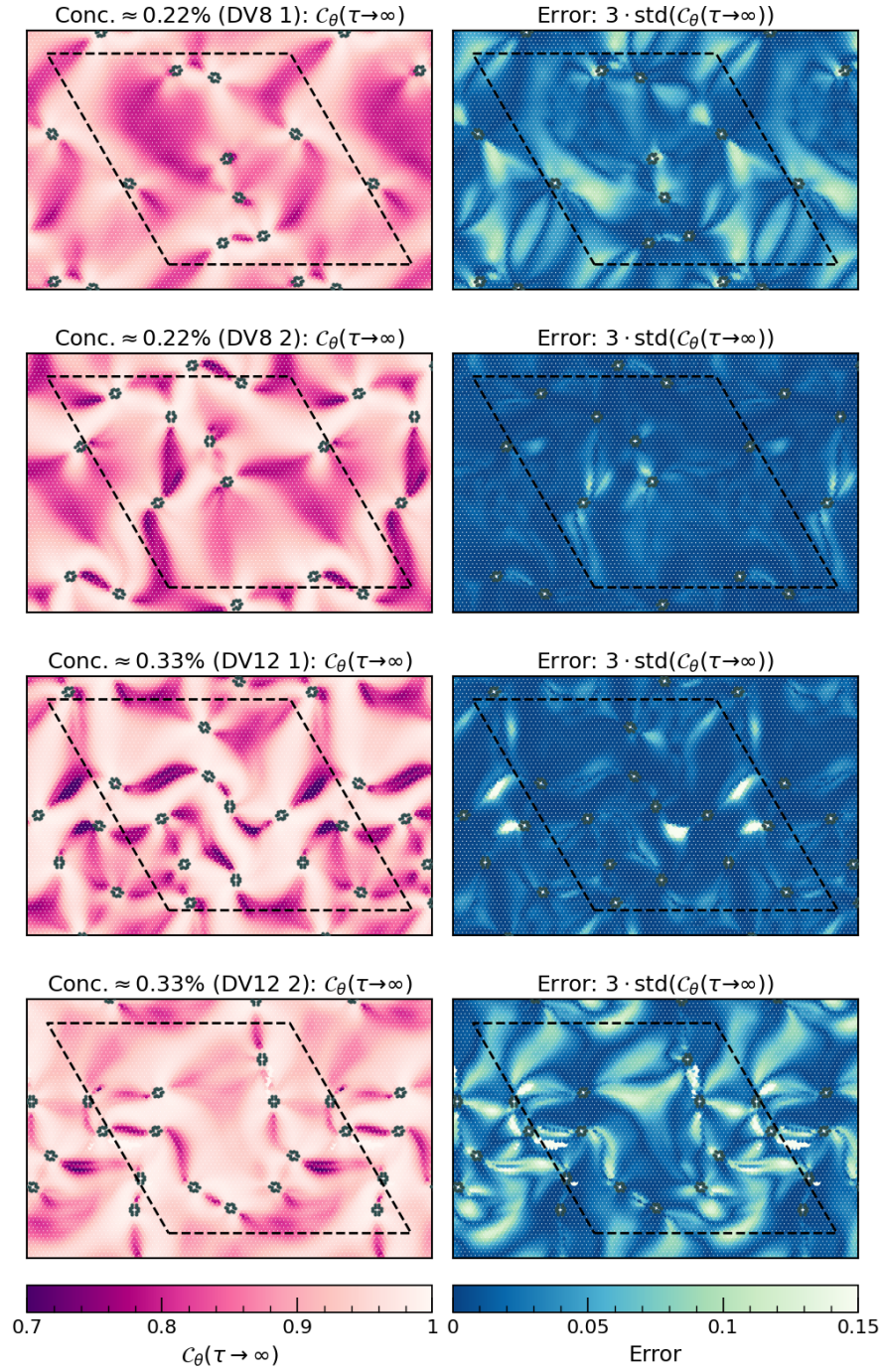


Figure S10. Atom-resolved plateau values of the angle autocorrelation function, $C_\theta(\tau \rightarrow \infty)$, for systems comprising between 8 and 12 divacancy defects corresponding to a defect concentration between $\approx 0.22\%$ and $\approx 0.33\%$. The atoms forming a divacancy are highlighted in grey. For each system we report the calculated atomic values (left) as well as the associated error based on the threefold standard deviation estimated via bootstrapping (right). White areas correspond to atoms where the prediction or error estimate are outside the color scale and are, thus, not reliable results.

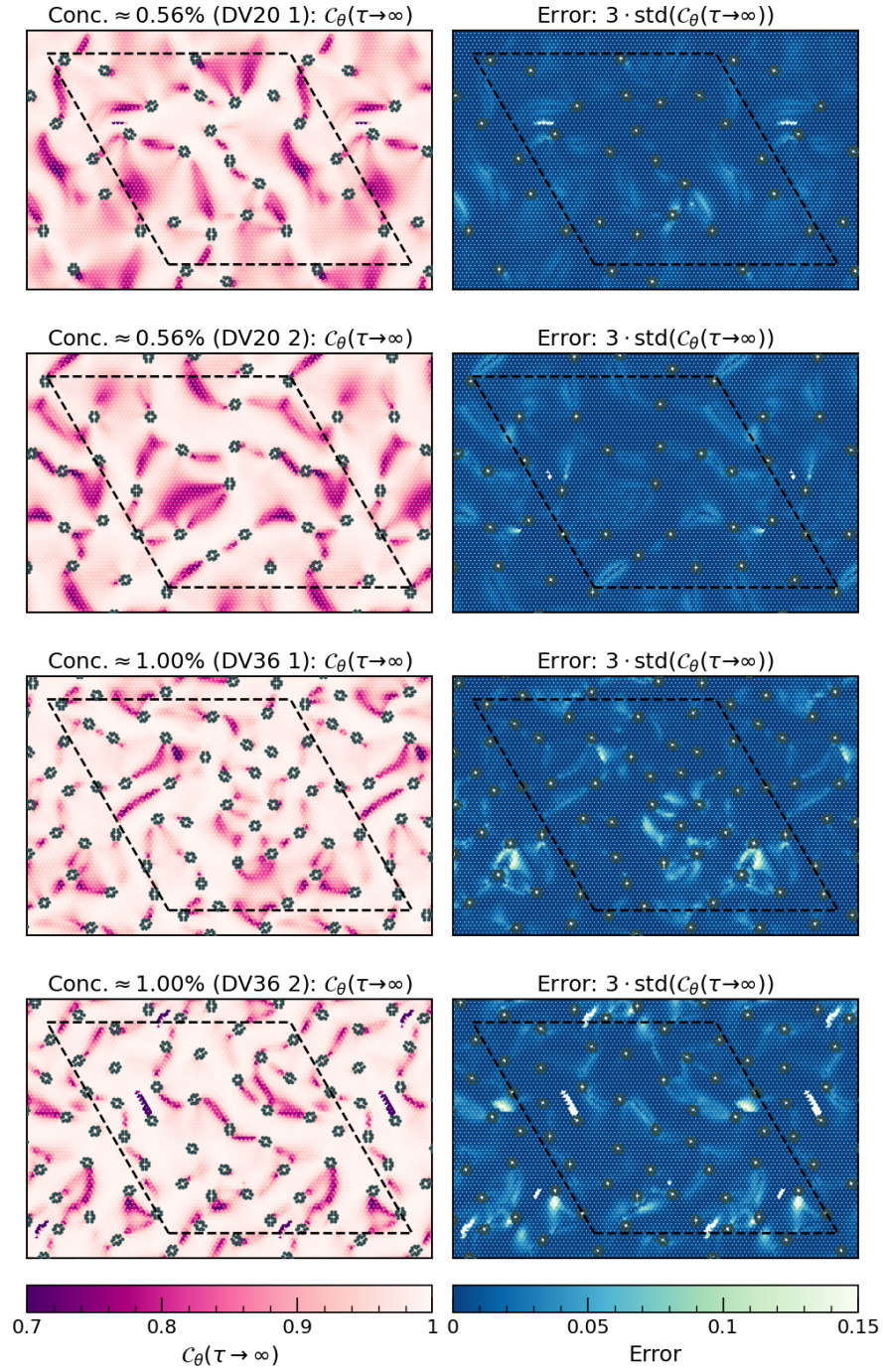


Figure S11. Atom-resolved plateau values of the angle autocorrelation function, $C_\theta(\tau \rightarrow \infty)$, for systems comprising between 20 and 36 divacancy defects corresponding to a defect concentration between $\approx 0.56\%$ and 1% . The atoms forming a divacancy are highlighted in grey. For each system we report the calculated atomic values (left) as well as the associated error based on the threefold standard deviation estimated via bootstrapping (right). White areas correspond to atoms where the prediction or error estimate are outside the color scale and are, thus, not reliable results.

S3 SENSITIVITY OF THE OBTAINED RESULTS

In this section, we assess the reliability of our results through convergence tests concerning the system size and simulation time. Then, we compute and discuss alternative measures reported in the literature to quantify the static and dynamic behavior of ripples.

S3.A Convergence tests

S3.A.1 System size

We start our convergence analysis by examining the impact of the system size on the results reported in the manuscript. It is well-established in the theory of flexible membranes⁵⁻⁷ that the average amplitude of the ripples exhibits a power-law scaling with the dimensions of the system. Here, we explore how the measures introduced in the manuscript, namely the rms inclination, θ_{rms} , and the plateau value of the normalised angle autocorrelation function, $C_\theta(\tau \rightarrow \infty)$, depend on the system size by performing additional MD simulations on systems where the pristine sheet contains 1800 atoms. This corresponds to a quarter of the system size used in the simulations to produce the results reported in the manuscript. We employ the identical simulation setup as described in Section S1 S1.A, where all simulations are at least 800 ps in length, with the majority exceeding one nanosecond. To achieve defect concentrations comparable to those reported in the manuscript we introduce up to 9 divacancy defects, corresponding to a defect concentration of 1%. For each concentration investigated, we conduct three simulations, varying the arrangement of defects according to the constraints outlined in Section S1 S1.A. The only exceptions are the pristine graphene sheet and the lowest accessible concentration, where only one defect is induced.

The summary of our analysis is presented in figure S12, with the rms inclination, θ_{rms} , shown on the left and the dynamic measure, $C_\theta(\tau \rightarrow \infty)$, on the right, both as function of the defect concentration for both the original and the reduced system sizes. We note that the R^2 scores for fitting the exponential function in equation 8 to the normalized angle autocorrelation functions are expectedly slightly lower for smaller system sizes. Nevertheless, we still obtain reliable fits, with R^2 scores above 0.9 for the large majority of cases, and the minimum score above 0.75. Similar to the results reported in the manuscript, we observe a discontinuity in both measures for the smaller

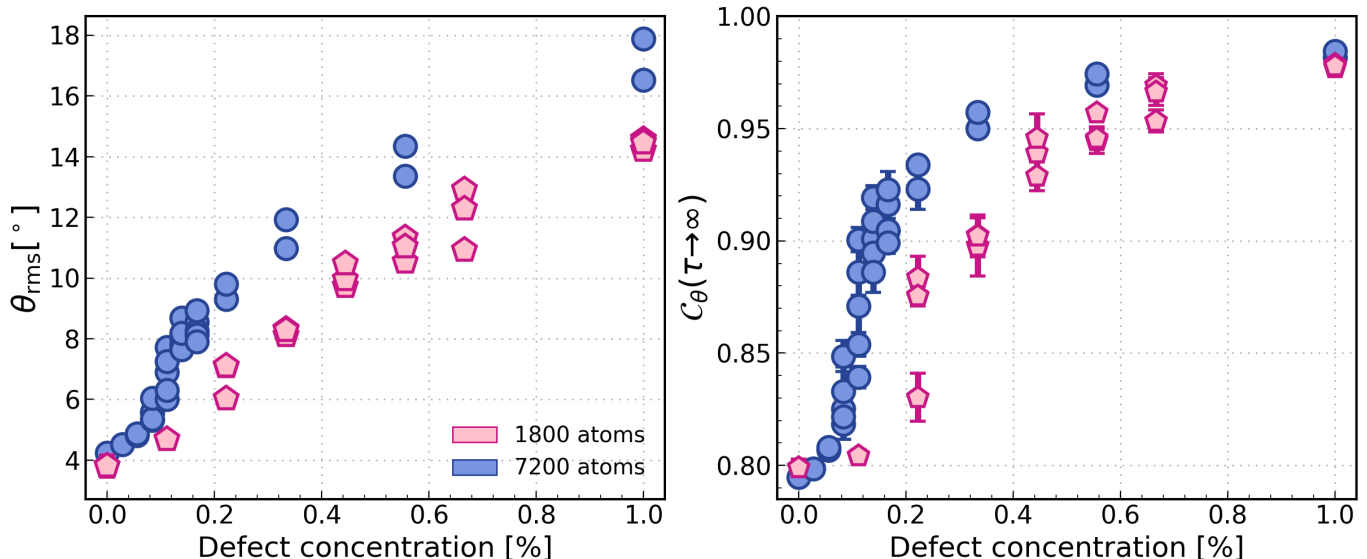


Figure S12. Impact of system size on static and dynamic behaviour of pristine and defective graphene. The two panels show the rms inclination (left) and the plateau value of normalised angle autocorrelation function (right) as function of the defect concentration for two system sizes with the pristine reference systems containing 1800 and 7200 atoms, respectively. The data computed for the larger systems is identical to the data reported in the manuscript in Fig 2(a). The statistical error was computed for each system based on bootstrapping using four blocks and is visualised by the error bars to the threefold standard deviation.

systems, with the discontinuity being more pronounced in the dynamics of the system. With decreasing system size, the phase transition shifts to larger defect concentrations of $\approx 0.2\%$, establishing our reported concentration in the manuscript of $\approx 0.1\%$ as the upper boundary for graphene sheets with sizes of the order of $1 \mu\text{m}$, as utilised in experiments.⁸ This analysis raises concerns about direct comparisons between ab initio molecular dynamics (AIMD) studies and experimental observations on defective graphene. While the former may suggest that the membrane maintains liquid-like ripples even with the introduction of a single defect, experiments conducted on larger graphene sheets at the same defect density are expected to result in highly buckled structures.

Finally, we briefly discuss the implications of our analysis for pristine graphene. In fact, in the absence of defects, both measures appear to be independent of the system size. At first glance, this may seem to contradict the scaling relation observed in both MD simulations⁹ and electron diffraction experiments,¹⁰ where the rms inclination, θ_{rms} , scales exponentially with the system size of the freestanding graphene sheet, L , according to $\theta_{\text{rms}} \propto \exp(-l/L)$. However, our results can be reconciled with these findings by understanding the parameter l as the inverse resolution of the measurement. While in TEM experiments¹⁰ l corresponds to the electron coherence length, typically in the range of $5 - 20 \text{ nm}$,⁸ the computational study⁹ obtains the average angle of a small region of graphene via Gaussian interpolation, and l represents the width of the Gaussian. In this work, conversely, we do not perform any spatial averaging of the normal angle; instead, we compute the normal angle exclusively at the center of each atom, and the rms inclination of the system is based on the ensemble average of these atomic angles as defined in equation 5. Framing this in the approach used in,⁹ instead of using Gaussians, we work with Dirac functions corresponding to $l = 0$. In line with the scaling relation, this results in the same estimate of θ_{rms} irrespective of the system size. Given the low ratios employed in TEM measurements, with commonly used electron coherence lengths of $5 - 20 \text{ nm}$ and graphene dimensions of $\approx 1 \mu\text{m}$ resulting in $l/L \leq 0.02$, this enables a direct comparison of our results with experiments.

S3.A.2 Simulation time

In this section we investigate the sensitivity of our results with respect to the length of our MD simulations. To this end, we recompute the rms inclination, θ_{rms} , and the plateau value of the normalised angle autocorrelation

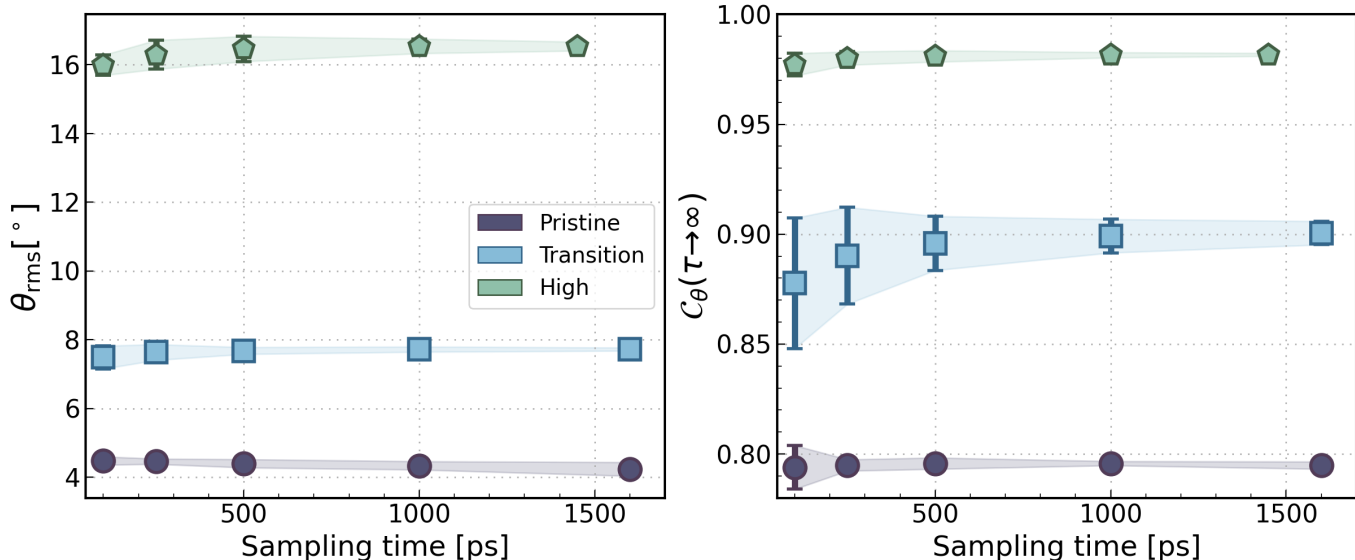


Figure S13. Analysis of the convergence of static and dynamic behaviour of pristine and defective graphene with respect to the simulation time. The two panels show the rms inclination (left) and the plateau value of normalised angle autocorrelation function (right) against the sampling time for three distinct systems with varying defect concentration. In addition to a pristine sheet (*Pristine*), we analyse the convergence for graphene samples at the critical defect concentration of $\approx 0.1\%$ corresponding to 4 defects (*Transition*) and the most defective sample with 36 defects corresponding to a concentration of 1.0% (*High*). Values for the longest sampling times (around 1.5 ns) correspond to Fig 2(a) in the manuscript. Statistical errors, computed via bootstrapping using four blocks, are depicted with error bars, reflecting the threefold standard deviation, along with shaded areas.

function, $\mathcal{C}_\theta(\tau \rightarrow \infty)$, for a set of shorter sampling times $t_{\text{sampling}} = \{100, 250, 500, 1000\}$ ps. We then compare these values with those reported in the manuscript for three different systems with varying defect concentrations. These systems encompass the pristine reference, the highest defect concentration of 1.0% (36 defects), and a sample at the critical defect concentration of $\approx 0.1\%$ (4 defects), where the phase transition occurs. The original computations for all of these systems were conducted over sampling times of approximately 1.5 ns. A summary of this convergence analysis is shown in figure S13.

For both properties, the qualitative differences between the three systems remain apparent regardless of the simulation time. The rms inclination shows hardly any dependence, with the deviation between lowest and longest sampling time being below 5% for all systems being. The plateau value of the normalised angle autocorrelation function, $\mathcal{C}_\theta(\tau \rightarrow \infty)$, conversely, shows a slightly stronger dependence for the graphene system at the critical defect concentration. Naturally, dynamical properties are inherently more challenging to converge which is also reflected in a higher uncertainty denoted by the larger errorbars. However, for all three systems both properties seem to have plateaued at a simulation length of 1 ns. Considering our shortest sampling time is 850 ps, and the majority of our simulations exceed 1 ns in duration, we can conclude that our results are sufficiently converged and allow for a quantitative comparison between the all systems.

S3.B Alternative observables

The objective of this section is to validate the robustness of our results by comparing the measures established in the manuscript to alternative observables. To this end, we first compare our rms inclination to the corrugation amplification factor (CAF) introduced in reference.² Subsequently, we will also compute the mean-squared displacement (MSD) in the direction perpendicular to the sheet and the velocity probability density function (PDF) which have been reported for pristine graphene in reference.¹¹

S3.B.1 Corrugation amplification factor

The corrugation amplification factor (CAF) aims to quantify the corrugation of a graphene sheet with respect to the pristine reference. Specifically, the CAF represents the ratio of the standard deviation of the atomic heights distribution sampled over all atoms and frames of a system relative to that observed for pristine graphene. For a more

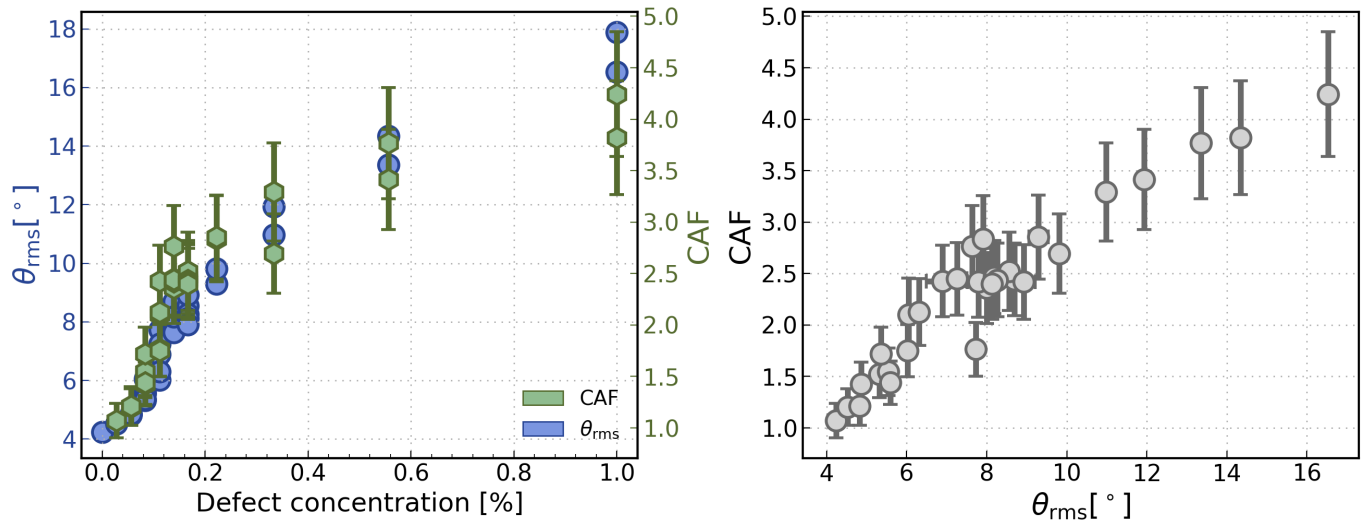


Figure S14. Comparison between the rms inclination and the corrugation amplification factor (CAF) introduced in reference.² The left panel shows both the CAF and the rms inclination as a function of the defect concentration. Note that the CAF for pristine graphene is 1 and not shown here. The data reported for the rms inclination is identical to that reported in the manuscript in figure 2a. To better understand the relationship between the two measures, the right panel displays the correlation between the two quantities. For both properties, the statistical errors were computed via bootstrapping using four blocks and are depicted with error bars, reflecting the threefold standard deviation.

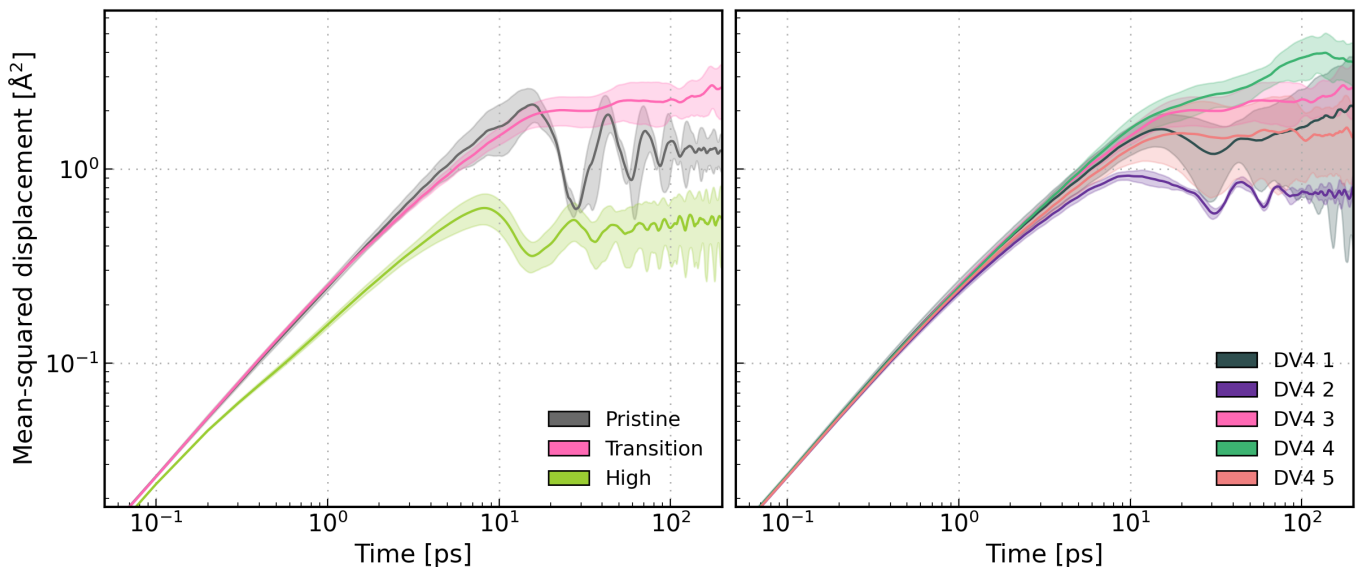


Figure S15. Mean-squared displacement (MSD) of the graphene sheet height as a function of time. The left panel shows the MSD for three distinct systems with varying defect concentration. In addition to a pristine sheet (*Pristine*), we analyse the convergence for graphene samples at the critical defect concentration of $\approx 0.1\%$ corresponding to 4 defects (*Transition*) and the most defective sample with 36 defects corresponding to a concentration of 1.0% (*High*). The right subplot, conversely, displays the MSD for different spatial realisations of the critical defect concentration. The shaded areas represent the statistical error corresponding to the standard deviation estimated via block averaging over 4 blocks.

comprehensive explanation the reader is referred to the original reference.² Here, we compute the CAF for all systems studied in the manuscript and an overview of the results and a comparison to the rms inclination is shown in figure S14.

Starting with the left panel of figure S14, we find that the CAF and the rms inclination exhibit a very similar dependence on the defect concentration. Specifically, the defect concentration with highest variance across different spatial arrangements is identical for both quantities. However, the CAF exhibits a significantly larger statistical error. This can be attributed mainly to two factors: First, the propagation of uncertainty inherently induced by relating all measurements to the value computed for pristine graphene. Second, by assuming the atomic heights follow a unimodal normal distribution which may not be accurate for highly defective systems. Note that compared to the original reference,² here we use a more conservative error estimate by taking the three-fold standard deviation obtained from bootstrapping over 4 blocks rather than the single standard deviation derived from block averaging over 20 blocks. Despite these shortcomings, the CAF seems to qualitatively confirm the well-converged results based on the rms inclination. In fact, as shown in the left panel of figure S14, there is a strong correlation between the two quantities.

S3.B.2 Mean-squared displacement

Turning now to an alternative measurement to quantify the dynamics of the system, here we focus on the mean-squared displacement (MSD) of the graphene sheet perpendicular to the surface. Previous experiments on pristine graphene¹¹ observed two distinct regimes where superdiffusive and subdiffusive motion dominated at short and long times, respectively. Here, we compute the MSD over 200 ps for the same set of systems as in section S3.S3.A S3.A.2, ranging from pristine graphene to the highest defect concentration of 1.0% (36 defects). To understand the sensitivity of the MSD with respect to the arrangements of defects, we further analyse the MSD for all samples at the critical defect concentration of $\approx 0.1\%$ (4 defects). Due to the large time scale, here we compute the statistical error based on the standard deviation obtained via block averaging over 4 blocks rather than performing bootstrapping. A summary of the obtained results is depicted in figure S15 with both the MSD and the time represented on a logarithmic scale.

Similar to the experiments,¹¹ we observe two distinct regimes for pristine graphene (*Pristine*): rapid diffusion at short time scales and to slow motion at longer scales. For times ≥ 10 ps we observe damped periodic oscillations which can be attributed to the finite size of our simulation box and their frequency intrinsically dependent on the

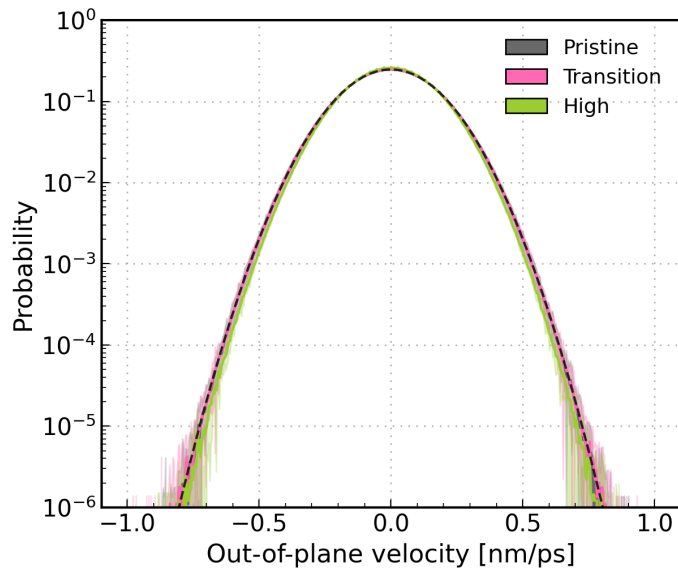


Figure S16. Probability distribution of the atomic velocities perpendicular to the graphene sheet. In addition to a pristine sheet (*Pristine*), we analyse the convergence for graphene samples at the critical defect concentration of $\approx 0.1\%$ corresponding to 4 defects (*Transition*) and the most defective sample with 36 defects corresponding to a concentration of 1.0% (*High*). The dashed black line corresponds to a Gaussian fitted to the data of the *Pristine* system. The statistical errors were computed via bootstrapping using four blocks and are depicted with the shaded areas, reflecting the threefold standard deviation.

system size. The most defective system (*High*) shows overall a very similar behaviour compared to pristine graphene, with the exception of a slower diffusion at shorter time scales and a shift towards lower MSDs in the long-term limit. This agrees well with our findings indicating a less mobile system at large defect concentrations. Most intriguing, however, is the behaviour of the system at the critical defect concentration (*Transition*): While it mimics the motion of pristine graphene at short time scales, the MSD converges to a larger value without showing the oscillations observed for the two other systems.

To better understand these findings, the left subplot of figure S15 displays the MSD as a function of time for all spatial realisations of the critical defect concentration studied in this work. While all systems seem to behave indetically at short time scales, they vary significantly at times ≥ 10 ps. In particular, one of the systems, denoted as DV4 2, displays a comparable pattern to the highly defective reference system, characterised by oscillations and ultimately converging to a MSD lower than that of pristine graphene. Interestingly, DV4 2 exhibits the largest value of $\mathcal{C}_\theta(\tau \rightarrow \infty) \approx 0.9$ (cf. figure S3) at this given concentration. This suggests a direct relationship between the MSD, and thus, the mobility of the system, with the introduced plateau value of the angle autocorrelation function. Moreover, relatively larger MSDs in the long-time limit indicate that with increasing defect concentration the system first becomes more mobile, at least locally, before, converging to a highly static pattern. Furthermore, the relatively larger MSDs in the long-time limit suggest that with increasing defect concentration, the system initially becomes more mobile, at least locally, before eventually converging to a highly static pattern when more defects are introduced. This aligns well with our findings regarding local areas of high mobility, as demonstrated in the atomic heatmaps analysed in the previous section and depicted in Figure 3 of the manuscript.

S3.B.3 Velocity probability distribution

Considering the experimental reports¹¹ suggesting that the out-of-plane velocity of pristine graphene follows a Cauchy-Lorentz distribution rather than a Normal distribution, we proceed to compute the velocities of the atoms in the direction perpendicular to the sheet using finite differences. We then compute the probability distribution over all atoms and frames where we employ bootstrapping with 4 blocks to estimate the statistical error. In an analogous fashion the previous sections, this analysis is carried out for three different systems with varying defect concentrations. These systems include the pristine reference, the highest defect concentration of 1.0% (36 defects), and a sample at the critical defect concentration of $\approx 0.1\%$ (4 defects). A summary of our results is displayed in figure S16. In contrast to the experiments, we find that all graphene membranes follow a Normal distribution irrespective of their defect

concentration.

REFERENCES

- ¹P. Rowe, V. L. Deringer, P. Gasparotto, G. Csányi, and A. Michaelides, “An accurate and transferable machine learning potential for carbon,” *Journal of Chemical Physics*, vol. 153, p. 034702, 2020.
- ²F. L. Thiemann, P. Rowe, A. Zen, E. A. Müller, and A. Michaelides, “Defect-Dependent Corrugation in Graphene,” *Nano Letters*, vol. 21, no. 19, pp. 8143–8150, 2021.
- ³S. Plimpton, “Fast Parallel Algorithms for Short-Range Molecular Dynamics,” *Journal of Computational Physics*, vol. 117, no. 6, pp. 1–19, 1995.
- ⁴U. Ludacka, M. Monazam, C. Rentenberger, M. Friedrich, U. Stefanelli, J. Meyer, and J. Kotakoski, “In situ control of graphene ripples and strain in the electron microscope,” *npj 2D Materials and Applications*, vol. 2, no. 1, p. 25, 2018.
- ⁵D. R. Nelson and L. Peliti, “Fluctuations in Membranes With Crystalline and Hexatic Order.,” *Journal de physique Paris*, vol. 48, no. 7, pp. 1085–1092, 1987.
- ⁶P. Le Doussal and L. Radzihovsky, “Self-consistent theory of polymerized membranes,” *Physical Review Letters*, vol. 69, no. 8, pp. 1209–1212, 1992.
- ⁷D. R. Nelson, T. Piran, and S. Weinberg, eds., *Statistical Mechanics of Membranes and Surfaces*. Singapore: World Scientific, 2 ed., 2004.
- ⁸J. C. Meyer, A. K. Geim, M. I. Katsnelson, K. S. Novoselov, T. J. Booth, and S. Roth, “The structure of suspended graphene sheets,” *Nature*, vol. 446, no. 7131, pp. 60–63, 2007.
- ⁹A. K. Singh and R. G. Hennig, “Scaling relation for thermal ripples in single and multilayer graphene,” *Physical Review B - Condensed Matter and Materials Physics*, vol. 87, p. 094112, Mar 2013.
- ¹⁰R. Singh, D. Scheinecker, U. Ludacka, and J. Kotakoski, “Corrugations in free-standing graphene,” *Nanomaterials*, vol. 12, no. 20, 2022.
- ¹¹M. L. Ackerman, P. Kumar, M. Neek-Amal, P. M. Thibado, F. M. Peeters, and S. Singh, “Anomalous dynamical behavior of freestanding graphene membranes,” *Physical Review Letters*, vol. 117, p. 126801, Sep 2016.